ACS OMEGA

http://pubs.acs.org/journal/acsodf

Article

Efficient Removal of Phosphate from Wastewater by a Novel Phyto-Graphene Composite Derived from Palm Byproducts

Nourhan El-Maghrabi,* Manal Fawzy, and Alaa El Din Mahmoud

Cite This: *ACS Omega* 2022, 7, 45386−45402

Read Online

ACCESS | Metrics & More | Article Recommendations | Supporting Information

ABSTRACT: The increased demand for clean water especially in overpopulated countries is of great concern; thus, the development of eco-friendly and cost-effective techniques and materials that can remediate polluted water for possible reuse in agricultural purposes can offer a life-saving solution to improve human welfare, especially in view of climate change impacts. In the current study, the agricultural byproducts of palm trees have been used for the first time as a carbon source to produce graphene functionalized with ferrocene in a composite form to enhance its water treatment potential. Scanning electron microscopy (SEM), energy-dispersive X-ray spectroscopy, X-ray diffraction (XRD), ultraviolet−visible, Fourier transform infrared spectroscopy, zeta potential, thermogravimetric analysis, and Raman techniques have been used to characterize the produced materials. SEM investigations confirmed the formation of multiple sheets of the graphene composite. Data collected from the zeta potential revealed that graphene was supported with a negative surface charge that maintains its stability while XRD elucidated that graphene characteristic peaks were evident at 2θ = 22.4 and 22.08° using palm leaves and fibers, respectively. Batch adsorption experiments were conducted to find out the most suitable conditions to remove PO_4^{3-} from wastewater by applying different parameters, including pH, adsorbent dose, initial concentration, and time. Their effect on the adsorption process was also investigated. Results demonstrated that the best adsorption capacity was 58.93 mg/g (removal percentage: 78.57%) using graphene derived from palm fibers at 15 mg L^{-1} initial concentration, pH = 3, dose = 10 mg, and 60 min contact time. Both linear and non-linear forms of kinetic and isotherm models were investigated. The adsorption process obeyed the pseudo-second-order kinetic model and was well fitted to the Langmuir isotherm.

1. INTRODUCTION

Despite phosphorous being a mineral nutrient that is essential for plant growth, it is considered a major pollutant because it can accumulate and reach dangerous concentrations in water bodies due to agricultural, domestic, and industrial discharge causing eutrophication in many water courses.[1] Both developed and developing countries, especially mega agricultural ones, such as China, the United States, Brazil, and India, suffer from excessive concentrations of phosphorus and other nutrients in their wastewater.[2] Most municipal wastewater treatment plants cannot efficiently remove phosphate from their effluents.[3,4] As such, eutrophication is a worldwide serious environmental problem caused as a result of nutrient enrichment in water bodies. The algal bloom that is associated with eutrophication poses a serious threat to the sustainability of aquatic ecosystems and drinking water safety.[5] Phosphate concentrations higher than 0.02 mg L^{-1} can cause eutrophication.[6] The recovery of a water body subjected to eutrophication is a very slow process. Thus, researchers seek to find effective ways to remove phosphate from wastewater.[7]

Agricultural wastes remain a challenging problem because of their accumulations, difficulties in its transportation, handling, and storage; moreover, converting the wastes into feedstock is an expensive process.[8] Agricultural wastes are renewable resources that can be used to produce various carbon materials; they are regenerative precursors, available, not expensive, produce a large yield, and are environmentally friendly.[9] Carbonization is the process of heating the biomass (pyrolysis) at high temperatures, above 200 °C, in the absence of air.[10] It usually produces biochar that is a carbon-enriched, porous, and grayish-black solid[11,12] and involves the transformation of sp^3 C−X bonds into the aromatic sp^2 C−C bonds.[13]

Some agricultural wastes have been used in the synthesis of different forms of carbon nanomaterials, such as porous graphene nanosheets that were synthesized from coconut shells,[14] N-doped graphene from chitosan extracted from crustacean skin wastes,[15] graphene quantum dots from dead

Received: September 15, 2022
Accepted: November 22, 2022
Published: November 30, 2022

https://doi.org/10.1021/acsomega.2c05985
ACS Omega 2022, 7, 45386−45402

neem leaves (*Azadirachta indica*),[16] 3D graphene from the wood of *Eucalyptus robusta* and sugarcane bagasse,[17] the Ag−Cu/biochar nanocomposite from *Atriplex halimus* biomass,[18] and 2D porous graphene nanosheets from cornstalk pith.[19] Graphene was also synthesized by *Colocasia esculenta* and *Nelumbo nucifera* leaves.[9] Porous carbon nanoparticles were recently synthesized from garlic peels,[20] activated carbon was prepared from the palm kernel shell,[21] silver-functionalized biochar was synthesized from *Chenopodium ambrosioides* biomass,[22] porous-activated carbon synthesized from arhar stalks,[23] and carbon quantum dots were produced from the corn stalk shell.[24]

Pyrolysis of biomass can produce highly porous graphene.[25] Methods of biomass pyrolysis may involve post-exfoliation,[26] template confinement,[27] salt-based,[28] hydrothermal carbonization pretreatment,[29] and chemical blowing.[30] Table S1 illustrates the pros and cons of the above-mentioned techniques.

The salt-based method uses salts because of their powerful effect on the activation of the produced material, providing a liquid reaction environment and shape fixing. Various salts can be used, such as KOH, H_3PO_4, $ZnCl_2$, K_2CO_3, and NaOH.[31] Among the salts that can be used is ferrocene. It is an organometallic compound with the molecular formula $Fe(\eta^5\text{-}C_5H_5)_2$. Iron is sandwiched between two cyclopentadienyl rings in staggered conformation (Figure S1).[32] Ferrocene is stable in the air and sublimes at temperatures above 100 °C. The stability of the ferrocene molecule is explained on the basis of the molecular orbital theory.[33]

The use of ferrocene in the functionalization of graphene has been reported by Teimuri-Mofrad et al.;[34] however, they have synthesized graphene using hydrazine monohydrate, which is a toxic reducing agent. Ashwin Karthick et al. have synthesized graphene oxide (GO) ferrocene nanocomposites by mixing the two solutions of GO and ferrocene under 60 °C but it consumed a long time (6 h).[35] From these wet techniques that have difficulties eliminating the defects on the graphene sheets because of the harsh nature of the reducing agents and agglomeration of nanomaterials in organic solvents, Tamilselvi et al. added ferrocene to the coconut shell and coconut coir biomass powder to produce reduced GO.[36]

The adsorption technique has been used for several years for the recovery of phosphorus-polluted water because of its high efficiency, cost-effectiveness, reliability, and simplicity.[37] Several adsorbent materials were used, such as Fe and Al oxyhydroxides.[38] Liu and his team have used a graphene-zero-valent iron composite synthesized by a chemical reducing agent in phosphorus removal from aqueous solution,[4] while Jun et al.[39] and Koo et al.[40] used chemically synthesized GO; nevertheless, no literature has used graphene derived from palm biomass in the removal of phosphate. The use of graphene composites synthesized from agricultural waste is significantly efficient because it offers renewable, non-toxic, and low-cost bio-adsorbents. The agricultural wastes are unable to adsorb phosphate by themselves, but converting it to graphene composites enhances their adsorption capacities due to a great deal of hydroxyl existing in the hemicelluloses, lignin, and cellulose of agricultural products. Furthermore, the carboxyl groups can bind cations via ion exchange while combining graphene with metals makes it attractive for anions.[41] Such graphene composites possess greater adsorption capacity than conventional adsorbents, as graphene provides a high active surface area, largely delocalized π-electrons, unique nanostructures, adjustable chemical features, mechanical stability, and tailorable surface properties.[42] Decoration of graphene with metals does not offer only the properties of each component but it also creates new unique physicochemical properties and functions from the interaction between them when compared to the use of either material alone.[43] It helps in stabilizing the produced graphene and increasing the surface area because the presence of metals increases the distance between the graphene layers, which makes the two faces available for the reaction and prevents aggregation. Moreover, combining graphene with metals does not need molecular linker metals to be homogenously dispersed on its surface with high selectivity and reactivity, which increases the affinity of the composite toward capturing phosphate molecules.[44,45] Herein, the biomass of palm old leaves and fibers have been carbonized through the pyrolysis process with the aid of ferrocene to synthesize the graphene composite, which was later tested to remove phosphate from aqueous solutions and real wastewater. A comparison between the two plant parts in the removal efficiency of phosphate has been conducted along with the investigation of the effect of different parameters on the adsorption process.

2. MATERIALS AND METHODS

2.1. Preparation of the Plants' Biomass. The palm leaves and palm fibers were collected from the botanical garden of the Faculty of Science, Alexandria University. The different parts of the plant were washed with tap water then with deionized water (DW) and left for air drying followed by oven drying at 60 °C; then, it was allowed to cool in a desiccator. The dried plant biomass was ground into a fine powder (≤250 μm) by a stainless-steel grinder and stored in plastic containers to be used in further works.

2.2. Carbonization Using Ferrocene. Ferrocene (0.3 g) was added to 1.5 g of palm leaf powder and mixed well; afterward, it was heated in a muffle furnace at 250 °C for 10 min. The same procedure was adopted for palm fibers. The yields were denoted as L-G-F and F-G-F for carbonized palm leaves and palm fibers, respectively.

2.3. Carbonization without Ferrocene. Palm leaf and fiber powder of 1.5 g was carbonized in a muffle furnace at 250 °C for 1 h without the addition of ferrocene. This step was made only for the sake of comparison between the two types of graphene. L-G and F-G are acronyms for graphene from palm leaves and fibers, respectively. GO was synthesized by the modified Hummer method according to our previous work[46] for a comparison purpose as well.

2.4. Characterization. The crystalline structures of the synthesized graphene samples were elucidated by an X-ray diffractometer [Bruker, D8 Advance powder XRD] with Cu Kα radiation (40 kV and 40 mA). A scanning electron microscope [Hitachi, S-4800 FESEM] coupled with energy-dispersive spectroscopy (EDS) was utilized to observe the microstructures and elemental composition of the samples. Fourier transform-infrared (FTIR) spectra analysis was performed on a Nicolet 5700 FT-IR spectrometer [Thermo Fisher] with the standard KBr pellet method. UV−vis spectroscopy [Shimadzu, model no-UV 1800] was used to detect the optical properties of the synthesized graphene, while thermogravimetric analysis (TGA) was conducted by a TGA/DSC 2 instrument [Mettler Toledo] with a flow rate of 60 mL/min and heating rate at 10 °C/min. Zeta potential was conducted on triplicates using Zetasizer Nano ZS [Malvern

https://doi.org/10.1021/acsomega.2c05985
ACS Omega 2022, 7, 45386−45402

Panalytical]. Raman spectroscopy analysis was performed on a SENTERRA Raman spectrometer [Bruker-Germany] with a 514.5 nm excitation wavelength and power output of 10 mW at room temperature.

2.5. Batch Adsorption Experiments of Phosphorus Removal. *2.5.1. Experimental Procedure.* Batch experiments were carried out to investigate the effect of the pH (3−12), contact time (10−60 min), dose (0.01−0.05 g), and initial phosphate concentrations (5−25 mg L^{-1}) on the removal of phosphate from aqueous solutions. A stock solution of phosphate (100 mg L^{-1}) was prepared by dissolving potassium dihydrogen phosphate salt [KH_2PO_4] into 1000 mL DW, then serial dilutions were made to prepare different phosphate concentrations (5−25 mg L^{-1}), after that 5 mL of mixed reagent was added to 50 mL standard solutions, and after 5 min reaction period, a blue color was obtained (Figure 1).

Figure 1. Schematic diagram and photos of the plant biomass and the synthesized ferrocene-functionalized rGO using the pyrolysis method and its application in the removal of phosphate from wastewater.

After adding a definite biosorbent weight, the suspension was stirred at 200 r/min using an incubator shaker [HAF Teck, Egypt]; then, the absorbance and concentration were measured on UV−vis spectroscopy PG Instruments T80+, UK at λ_{max} = 880 nm while DW was used as a blank.

In order to prepare the mixed reagent, ammonium molybdate (15 g) was dissolved in 500 mL DW in a plastic bottle away from light (1), 140 mL sulfuric acid was diluted to 900 mL DW (2), 27 g ascorbic acid was dissolved in 500 mL DW and stored in a plastic bottle in a freezer (3), and 0.34 g antimonyl potassium tartrate in 250 mL DW (4). 100 mL of (1) was mixed with 250 mL of (2), 100 mL of (3), and 50 mL of (4) and was used no longer than 6 h from preparation.[47] All reagents are of analytical grade and were purchased from VWR chemicals, Belgium, except antimonyl potassium tartrate was from Loba Chemie Pvt Ltd, India. NaOH and HCl solutions of 0.1 M were used to adjust the pH; after equilibrium, the solutions were filtered by 0.2 μm pore size Whatman filter paper GF/A 47 mm to measure the remaining phosphate concentration.

To assess the recyclability of the adsorbents after the batch adsorption experiments, the phosphate-loaded adsorbent material was separated by filtration and mixed with 25 mL NaOH (1 M) desorbent solution for 2 h in a shaker to eliminate the adsorbed phosphate ions from the active sites of the graphene surface. Then, it was washed with DW to neutralize its surface and finally dried under vacuum conditions at 80 °C. 0.01 g of the treated adsorbent was dispersed in 50 mL of phosphate solution (15 mg L^{-1}, pH 3.0) followed by shaking for 1 h, then filtered, and transferred again into NaOH solution with shaking for 2 h. This procedure was repeated for four successive cycles.

Real effluent wastewater samples were collected from El Amya Drain, industrial, and agricultural wastewater, located in eastern Alexandria Governorate. Samples were immediately transported to the laboratory and treated with the synthesized graphene composites to demonstrate its applicability in phosphate removal. The concentration of phosphorus in the sample was 8.07 mg L^{-1}. The optimum examined conditions obtained from the batch adsorption experiments were implemented. The characteristics of the drain wastewater sample are shown in Table S4.

2.5.2. Adsorption Measurements. Removal efficiency and adsorption capacity were measured by eqs 1 and 2, respectively.[48,49] The linear form of pseudo-first-order, pseudo-second-order, and Elovich kinetic models (Table 1)

Table 1. Kinetic and Adsorption Isotherm Model Equations

kinetic/adsorption isotherm model	linear equation
pseudo 1st order	$\ln(q_e - q_t) = \ln q_e - K_1 t$
pseudo 2nd order	$\frac{t}{q_t} = \frac{1}{K_2 q_e^2} + \frac{t}{q_e}$
Elovich	$q_t = 1/\beta \ \ln(\alpha\beta) + 1/\beta \ \ln(t)$
	$C_e/q_e = 1/K_L q_m + C_e/q_m$
Langmuir	$R_L = \frac{1}{1 + K_l C_o}$
Freundlich	$\log(q_e) = \log(K_f) + \frac{1}{n}\log(C_e)$
Temkin	$q_e = B_T \ \ln K_T + B_T \ \ln C_e$
kinetic/adsorption isotherm model	**non-Linear equation**
pseudo 1st order	$q_t = q_e(1 - e^{-k_1 t})$
pseudo 2nd order	$q_t = \frac{q_e^2 K_2 t}{1 + K_2 q_e t}$
Langmuir	$q_e = \frac{q_m K_L C_e}{1 + K_L C_e}$
Freundlich	$q_e = K_f C_e^n$

was adopted to describe the mechanism and the rate of the adsorption process while Langmuir, Freundlich, and Temkin adsorption isotherm models (Table 1) were used to better understand the adsorption process.[48,50] The non-linear isotherm and kinetic models (Table 1) were also implemented.

$$R\ (\%) = \frac{C_o - C}{C_o} \times 100 \quad (1)$$

where R (%) is PO_4^{3-} removal efficiency (%) and C_o and C are the concentrations of PO_4^{3-} at zero and time t, respectively (mg L^{-1}).

$$q_e = \frac{(C_o - C_e) \times V}{m} \quad (2)$$

where q_e is the quantity of PO_4^{3-} adsorbed per unit mass adsorbent (mg/g), C_o is the initial concentration of PO_4^{3-}, C_e is the concentrations of PO_4^{3-} at equilibrium, V is the volume of solution (L), and m is the mass of the adsorbent material (g).

Where q_e, q_t, and q_m are the amount of phosphate adsorbed at equilibrium, at time t, and the maximum adsorption capacity

https://doi.org/10.1021/acsomega.2c05985
ACS Omega 2022, 7, 45386−45402

(mg/g), respectively. k_1 and k_2 are the rate constant of pseudo-first order (min^{-1}) and pseudo-second order (g mg^{-1} min^{-1}), respectively, and t is the contact time. β is the desorption coefficient (g mg^{-1}), and α is the initial adsorption rate (mg g^{-1} min^{-1}). C_e is the concentration at equilibrium (mg L^{-1}), K_L is the adsorption equilibrium constant (L mg^{-1}), R_L is the separation factor, and C_0 is the initial concentration (mg L^{-1}). K_f is the Freundlich constant (mg/g) and n is adsorption intensity. K_T is the equilibrium bond constant and B_T is the Temkin constant related to heat of sorption (J/mol) where $B = RT/b_T$: b_T is the Temkin constant of the adsorption heat (J/mol), R is the gas constant (8.3145 J mol^{-1} K^{-1}), and T is the absolute temperature at 303 K.

2.5.3. Data Analysis. All experiments were done in triplicate, and the results are represented as mean ± SD. The error bars indicating the standard deviation are shown wherever possible in the relevant figures. All data statistics, standard deviations, comprising means, and regressions (linear and non-linear) were computed on Microsoft Excel version 2207 and Origin pro software version 9.0.

3. RESULTS AND DISCUSSION

3.1. Characterization of the Synthesized Graphene.

3.1.1. Scanning Electron Microscopy Images. The dead plant biomass images (Figure 2a,b) show a highly porous morphology that enhances the fast heat transfer during the pyrolysis and leads to facilitating the experimental setup and increases the yield because at high temperatures, the carbon surfaces undergo cleavage and molecular arrangement, which leads to converting it into the graphene structure.[51] The surface morphology of the produced materials after carbonization and modification with ferrocene is shown in Figures 2c,d and S2. It was completely different from the plant biomass before modification. Both palm leaves and fibers have shown a sheet-like morphology with some wrinkles, which indicates the formation of graphene.[52] Moreover, the particles of ferrocene seem to be attached on the graphene surface with no separate particles being observed thus confirming the successful interaction and combination between them.[53] The scanning electron microscopy (SEM) images of palm fibers and leaves after pyrolysis without ferrocene (Figure 2e,f) presented a smooth sheet-like structure with some crinkles and ripples on the edge of these nanosheets, indicating that after the plant powder was subjected to relatively high temperatures its structures were exfoliated into thin micron-scale lateral size layers, which are the characteristic structure of graphene.[54,55]

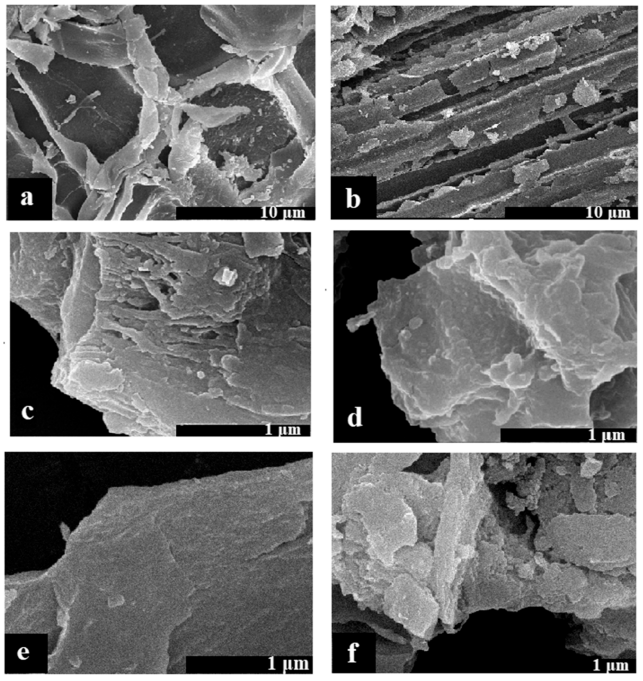

Figure 2. SEM images of the dead biomass of palm fibers (a) and palm leaves (b) before the carbonization process, F-G-F (c), L-G-F (d), F-G (e), and L-G (f).

3.1.2. X-ray Diffraction. X−ray diffraction (XRD) analysis of the palm leaves and fibers after the carbonization with ferrocene, as shown in Figure S3a, supports the formation of graphene by the appearance of a broad and intense diffraction peak at 2θ = 22.4° (d = 0.39 nm) and 2θ = 22.08° (d = 0.40 nm), respectively, that are corresponding to the 002 crystal plane signifying the re-establishment of the conjugated graphene network.[56] In addition, the palm fibers showed extra peaks at 2θ = 15.2, 29, 34, and 52°, while palm leaves demonstrated peaks at 2θ = 15, 29, and 49.5° that are indexed to the ferrocene characteristic diffraction peaks, which confirms the successful interaction between the produced graphene material and ferrocene.[34,57] However, ferrocene precursors aim to produce a Fe-based nanocomposite and low crystallinity of the iron species by XRD indicates the nanosized features of the particles.[58]

3.1.3. UV Analysis. UV−visible spectra of palm fiber extract (Figure S3b) indicate the presence of 232 and 265 nm peaks, while the palm leaf extract showed three absorption peaks at 232, 255, and 310 nm attributed to the phytoconstituents of flavonoids and their derivatives because the typical flavonoids show absorption peaks in the range of 230−285 and 300−350 nm.[59] In addition, bare ferrocene attained its characteristic 240 nm band that is related to the metal to legend charge transfer.[60] F-G-F and L-G-F acquired peaks at 275 and 265 nm, respectively, related to the $\pi-\pi^*$ transitions of the aromatic C═C bonds; nevertheless, a small shoulder band at 235 nm was observed in the F-G-F spectrum due to the carbonyl group (C═O) $n-\pi^*$ transitions that may be from the phytoconstituents.[61,62] This red shift in position that is different from the peaks of the plant extract and ferrocene confirms the formation of graphene as the absence of an absorption peaks near 300 nm proves the removal of oxygen-containing groups and the rearrangement of carbon atom order.[49] These results were also obtained by Tamilselvi et al. when they used coconut coir and coconut shell biomass in the synthesis of graphene[63] and is in line with many literature.[46,64−66]

3.1.4. FTIR Spectroscopy. The data obtained from FTIR spectroscopy (Figure S3c) elucidates the presence of many functional groups in the palm fiber biomass, such as O−H stretching at 3293 cm^{-1}, CH_2 at 2937 cm^{-1}, C═C vibrations at 1613 cm^{-1}, C═O stretching at 1537 cm^{-1}, C−H bending at 1408 cm^{-1}, C−O stretching of alkyl ether at 1239 cm^{-1}, and CO−O−CO stretching of anhydrides at 1025 cm^{-1}, which indicates the existence of many active compounds in the plant material and the possibility to be used as a carbon source.[67] FTIR spectra of graphene from palm fibers without ferrocene showed the presence of hydroxyl moieties at a slightly shifted position of 3252 cm^{-1}. Peaks at 2870, 1602, 1543, and 1060 cm^{-1} assigned to symmetric CH_2 stretching, C═C stretches,

https://doi.org/10.1021/acsomega.2c05985
ACS Omega 2022, 7, 45386−45402

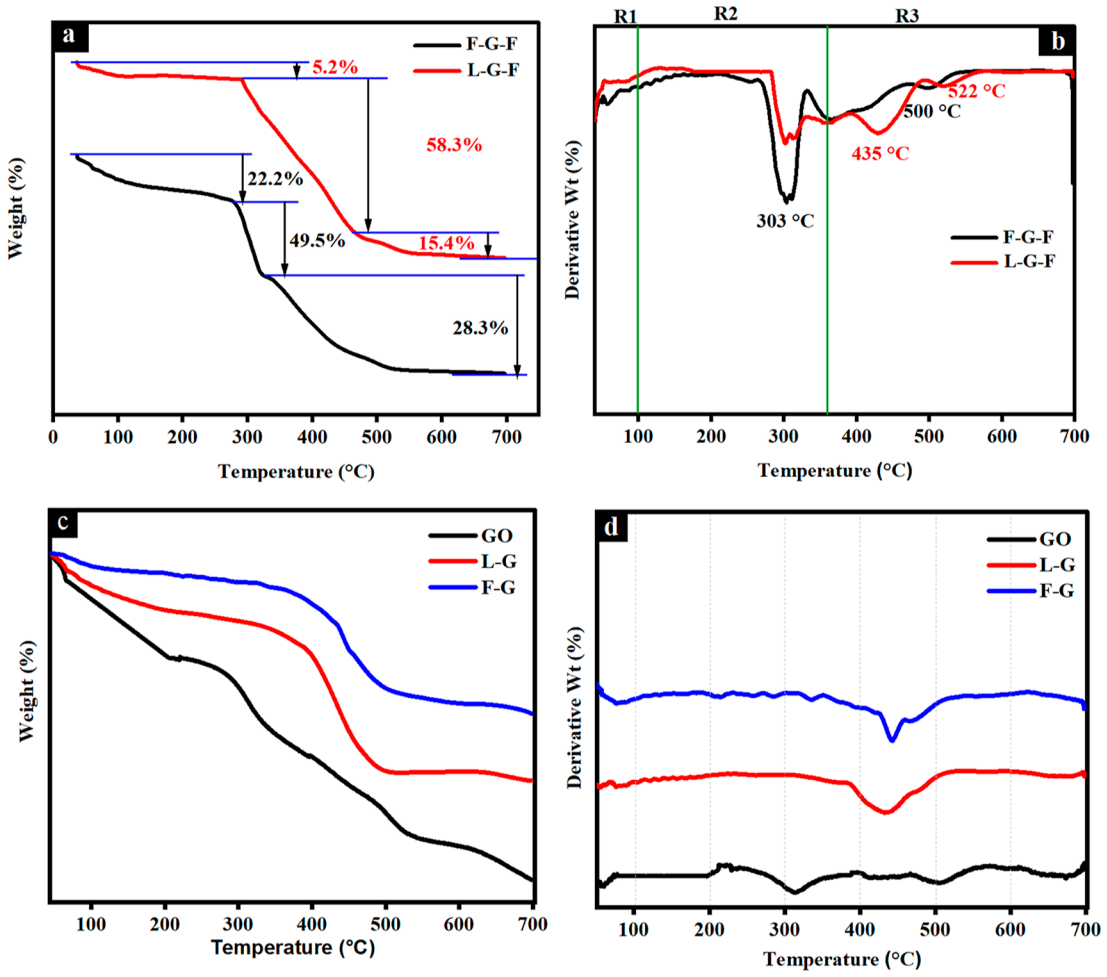

Figure 3. TGA (a) and DTG (b) of F-G-F and L-G-F. TGA (c) and DTG (d) of GO, F-G, and L-G.

C═O, and C−O stretching vibrations, respectively, were observed in lower intensities. The decrease in the number of oxygen-containing groups that were available in the plant biomass indicated the successful formation of graphene.[68] In comparison, after the addition of ferrocene and the pyrolysis process these absorption peaks have been shifted to slightly different positions as the O−H stretching appeared at 3276 cm^{-1}, H−C−H was at 2916 cm^{-1}, C═C vibrations shifted to 1634 cm^{-1}, and C−O−C stretching at 1021 cm^{-1}. Moreover, the peaks at 1537−1543 cm^{-1} that are assigned to C═O stretching disappeared. Such changes emphasize the successful interaction between the ferrocene and plant biomass during the carbonization process.[35,52] A similar trend was observed in palm leaves results that are in good agreement with other relevant studies.[53,66,69]

3.1.5. Zeta Potential. The zeta potential technique gives insights into the particles' tendency to aggregate by measuring the surface charge of the material. The level of the electrostatic repulsion reflects the stability of the material so the higher the value of the surface charge (positive or negative), the better dispersion, and stability.[70] The zeta potential of the prepared materials, as shown in Figure S3d, illustrates that L-G-F is acquired a negative charge of −21.3 mV; however, the F-G-F value was −23.4 mV, which may reflect the better stability and more negative functional groups attached to its surface. The appearance of such negative charges along with the visual observation of a homogenous solution in Figure S5a emphasizes the good dispersion and stability of the produced graphene.

3.1.6. Energy-Dispersive X-ray Spectroscopy. The elemental composition of the produced materials is shown in Figure S4. The elemental composition was mainly carbon and oxygen with the presence of other elements. L-G-F and F-G-F acquired high carbon mass percentages of 60.82 and 53.22%, respectively, while oxygen comes next with mass percents of 37.4 and 44.42%, respectively. The iron element was obviously present at different KeV thus confirming the effective attachment of ferrocene on the graphene plant material, whereas the existence of other elements, such as Mg, Si, K, and Ca may be from plant origin.[46] However, the elemental analysis of graphene without ferrocene showed that L-G and F-G have also a high carbon to oxygen ratio but without any presence of iron signals; thus, the iron content in the L-G-F and F-G-F is from the ferrocene addition. Also, the existence of other elements, such as Mg, Si, Cl, K, and Ca is due to the plant constituents.

3.1.7. TGA/Derivative Thermogravimetry Analysis. TGA analysis reveals the effect of material composition on its decomposition and its thermal stability; nevertheless, the derivative thermogravimetry T_{max} indicates the physical and chemical structure of the material. Generally, derivative thermo gravimetric analysis (DTG) is divided into three regions (R1−R3), R1 (temperature less than 100 °C) which is assigned to the evaporation of water, R2 (100−360 °C) referring to the

https://doi.org/10.1021/acsomega.2c05985
ACS Omega 2022, 7, 45386−45402

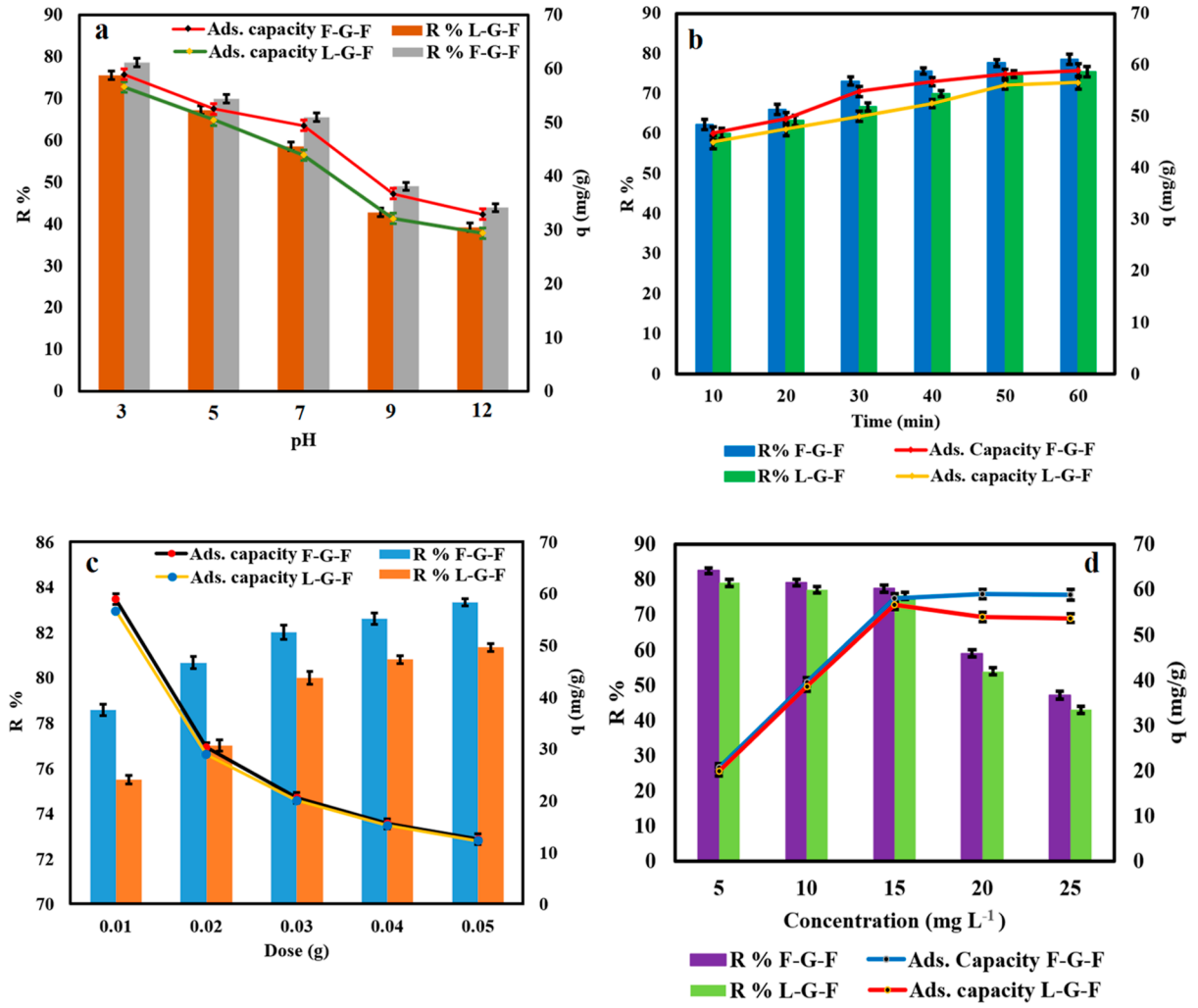

Figure 4. PO_4^{3-} removal efficiency and adsorption capacity of the synthesized phyto-graphene composites using different pH ranges (3−12), dose: 0.01 g, C_i: 15 mg L^{-1}, and temperature: 25 ± 2 °C for 60 min (a), impact of time (10−60 min) at experimental conditions of 0.01 g adsorbent dose, pH: 3, C_i: 15 mg L^{-1}, and temperature: 25 ± 2 °C (b), effect of different doses (0.01−0.05 g) at pH: 3, C_i: 15 mg L^{-1}, time: 60 min, and temperature: 25 ± 2 °C (c), and influence of PO_4^{3-} concentration (5−25 mg L^{-1}) at pH: 3, dose: 0.01 g, time: 60 min, and temperature: 25 ± 2 °C (d).

loss of oxygen-containing groups, and R3 (360−1000 °C) that represents carbon degradation.[71] TGA and DTG of L-G-F and F-G-F are shown in Figure 3a,b showing that L-G-F DTG has one peak at R2 of T_{max} = 303 °C and two other peaks at R3 of T_{max} = 435 and 522 °C; however, its TGA depicted that it was almost thermally stable till 300 °C as it lost only 5.2% of its weight and lost 58.3% when the temperature reached 470 °C. It did not completely degrade at 700 °C as it lost 79% of its weight. F-G-F TGA analysis presented a loss of 22.2% of the total weight at 300 °C and 100% at 700 °C with 3 DTG peaks at 303, 370, and 500 °C. In addition, GO and graphene from pyrolysis of palm fibers and leaves without ferrocene were also decomposed in comparison to F-G-F and L-G-F. Their TGA and DTG spectra are presented in Figure 3c,d. DTG measurements can be linked to the type of the graphene material, as graphene is a 2D sheet of carbon atoms that are arranged in a honeycomb structure and graphite is a result of many of these graphene sheets linked together with the van der Waals forces. Graphite takes more time and energy than any other graphene type to break those bonds as it starts to degrade in R3.[71] GO is the oxygenated version of graphene in which oxygen functional groups caused defects in the carbon structure and weakened the interaction between the graphene layers, so thermal degradation is much faster than any other form of graphene almost most of its weight is decomposed in R2 (Figure 3c,d), while reduced GO is its reduced form that can be distinguished from it by the higher stability and the less degradation in R2.[71] The results obtained in this study suggest that the synthesized material is reduced GO and the oxygen-containing groups can be from the phytoconstituents. Based on Zhou and his team, functional groups can be identified and quantified to the material based on its decomposition temperatures and thermal stabilities. Water trapped in the material or adsorbed on the surface is represented by the peak at 40−96 °C, while the peak at 96−160 °C is assigned to the alcoholic −OH loss of water through dehydration condensation reactions. Furthermore, the formation of phenol groups during the degradation of edge-plane oxygen-containing functional groups, such as carbonyl (C═O), epoxy, and carboxyl (−COOH) groups, is ascribed to the peaks at 160−250 °C. The sublimation of carbon frameworks and stable oxygen-containing moieties is in the stage of 250−333 °C; however, 333−523 °C is associated with the carbon nitride decomposition and 550−1000 °C depicts the degradation of

https://doi.org/10.1021/acsomega.2c05985
ACS Omega 2022, 7, 45386−45402

heptazine nitrides and sp^2 structures.[72,73] The mass loss % in each stage of the above-mentioned functional moieties has been calculated for all synthesized graphene derivatives (GO, L-G, F-G, L-G-F, and F-G-F) and listed in Table S2. The content of alcoholic −OH moieties among the five graphene materials is in the order of GO (16.45%), F-G-F (9.74%), L-G (9.16%), L-G-F (6.04%), and F-G (3.01%), while the content of oxygen-containing groups was as follows: GO (40.61%), F-G-F (12.9%), L-G (10.86%), L-G-F (8.64%), and F-G (6.43%). The carbon nitride structure content was L-G (51%), F-G (50.09%), L-G-F (49.2%), F-G-F (48.4%), and GO (13.93%), while the content of carbon sp^2 structures was F-G-F (24.25%), L-G-F (12.4%), L-G (10.5%), GO (9.28%), and F-G (7.65%). The remnant of each material was in the order of F-G (27.5%), L-G-F (21.21%), and L-G (11.68%) that may be decomposed in higher temperatures than 700 °C and is probably assigned to pure graphene structures.[73] It is obvious that the GO has the highest content of alcoholic −OH and oxygen-containing groups; nevertheless, the pyrolysis of the plant material in all other graphene materials has sharply decreased the content of such groups. Plant leaves are mainly composed of cellulose, hemi cellulose, and lignin. The cellulose tends to degrade between 314 and 500 °C, hemicellulose undergoes fast decomposition between 220 and 315 °C, and lignin is from 400 to 1000 °C with T_{max} around 600 °C;[51,74] subsequently, the TGA results of F-G-F and L-G-F confirm their composition of cellulose and lignin; such materials are a good carbon source and unlike pyrolysis on metal surfaces, its pyrolysis can be processed directly on their surface and at high temperatures, their carbon structure is rearranged, which leads to the formation of graphene.[75,76] Ferrocene degrades at the low-temperature range of 120−160 °C; however, ferrocene in composites starts to decompose at higher temperatures.[77] According to Figure 3, the materials started to degrade at far higher temperatures, which confirms the strong interaction between ferrocene and the carbon surface that is why much heat was required to break the strong pi−pi connection that stabilizes the composite. This observation also confirms that ferrocene is not just attached to the carbon surface but it has made a linkage that has changed the physical and chemical natures of each material.

3.1.8. Raman Analysis. Raman spectroscopy is the most nondestructive and direct analyses to describe the quality of carbon materials by confirming the defects and the ordered/disordered structures.[78] As shown in Figure S5b, GO, F-L-F, and L-G-F presented two featured peaks located at 1354, 1345, and 1347 cm^{-1} assigned to the D-band and at 1595, 1589, and 1587 cm^{-1} corresponding to the G-band.

The assignment of the D and G peaks is straightforward in the molecular picture of carbon materials. The D-band is associated with the radial vibration of carbon atoms and related to local defects and disorder in the honeycomb structure of the graphene nanosheets, while the G-band is related to the sp^2 carbon atom vibration in the 2D hexagonal lattice.[79] The shift in the D and G bands of GO to different positions in F-G-F and L-G-F is a clear indication toward the restoration of the sp^2 character and a higher order degree of graphene.[80,81]

The integral intensity ratio of I_D/I_G is proportional to the degree of graphitization of carbon materials and expresses a less defective structure when the intensity ratio is ≤ 1.[79] The value of I_D/I_G for GO, F-G-F, and L-G-F is calculated to be 0.97, 0.68, and 0.65, respectively. The reduction of the I_D/I_G value is attributed to the reduced disorder degree, suggesting a quite high graphitization degree of biographene, which is in accordance with the above XRD results.[54,82] The appearance of these peaks, the shift in their position, and the decrease of the I_D/I_G value confirm the successful fabrication of graphene.

3.2. Removal of Phosphate Using Different Parameters. *3.2.1. Effect of pH.* The adsorbate−adsorbent interaction generally depends on the species of the adsorbate and the surface charge of the adsorbent; thus, the pH value of aqueous solution plays a significant role in the adsorption process.[83] Herein, batch experiments have been conducted in the pH range 3−12 to investigate its effect on the removal efficiency and removal capacity of PO_4^{3-}. The experiment was conducted using 10 mg of the adsorbent material (L-G-F and F-G-F), initial concentration 15 mg L^{-1} of phosphorous solution, and contact time up to 60 min. Results available in Figure 4a show that the maximum removal efficiency (78.57%) was obtained using F-G-F graphene in the acidic medium at pH = 3, while increasing pH was accompanied with the decrease in the removal percentage to 43.87% at pH 12. The adsorption capacity has increased from 32.92 mg/g at pH 12 to 58.93 mg/g at pH 3. Phosphate can exist in different anionic species, such as H_2PO^{4-}, $H_2PO_4^{2-}$, and PO_4^{3-}; however, at the pH range 3−9 H_2PO^{4-} and HPO_4^{2-} are the main predominant forms.[84] Consequently, under acidic pH, the surface of the adsorbent material was positively charged so the active sites of the adsorbent would be favorable for phosphate adsorption due to the electrostatic interaction but when the pH value increased to 12, the OH^- and PO_4^{3-} species competed for active sites and decreased the removal efficiency.[85] It is obvious that F-G-F and L-G-F graphene has more or less the same performance; however, L-G-F showed slightly lower potentiality in the PO_4^{3-} removal as its maximum removal percentage and adsorption capacity was 75.55% removal and 56.6 mg/g, respectively, at pH = 3 and decreased to their minimum 39.16% and 29.37 mg/g at pH = 12. Using the unmodified graphene samples (F-G and L-G), as shown in Figure S6a, the removal efficiency has decreased from 63.66 to 61.42%, respectively, at pH = 3 to 34.62 and 33.3%, respectively, at pH = 12 while the adsorption capacity of F-G was 47.7 mg/g at pH = 3 and 26 mg/g at pH = 12. However, the adsorption capacity of L-G at pH 3 was 46.1 mg/g and decreased to 25 mg/g at pH 12. These results confirmed the positive effect for using ferrocene in enhancing the adsorption process. Finding the best pH environment to remove PO_4^{3-} from aqueous solution using the magnesium ferrite/biochar composite also depicted that the acidic medium, specifically at pH = 3, was the best condition.[84] These results are in line with many previous studies.[86−88]

3.2.2. Effect of Contact Time. The influence of time on the removal efficiency was investigated at different contact time of 10−80 min, material dose of 10 mg, initial concentration = 15 mg L^{-1}, at room temperature, and optimum examined pH of 3 using both materials F-G-F and L-G-F. Results from Figure 4b show that the percent removal has dramatically increased with increasing the contact time from 10 to 60 min using F-G-F; however, it stayed almost unchanged after 60 min. This increase in the removal percentage was accompanied with an increase in the adsorption capacity as well. The removal efficiency and adsorption capacity reached their maximum of 78.57% and 58.9 mg/g, respectively, after 1 h while they were only 62.27% and 46.7 mg/g after the first 10 min. L-G-F also indicated that increasing the contact time is responsible for enhancing the removal efficiency from 60% after 10 min to

https://doi.org/10.1021/acsomega.2c05985
ACS Omega 2022, 7, 45386−45402

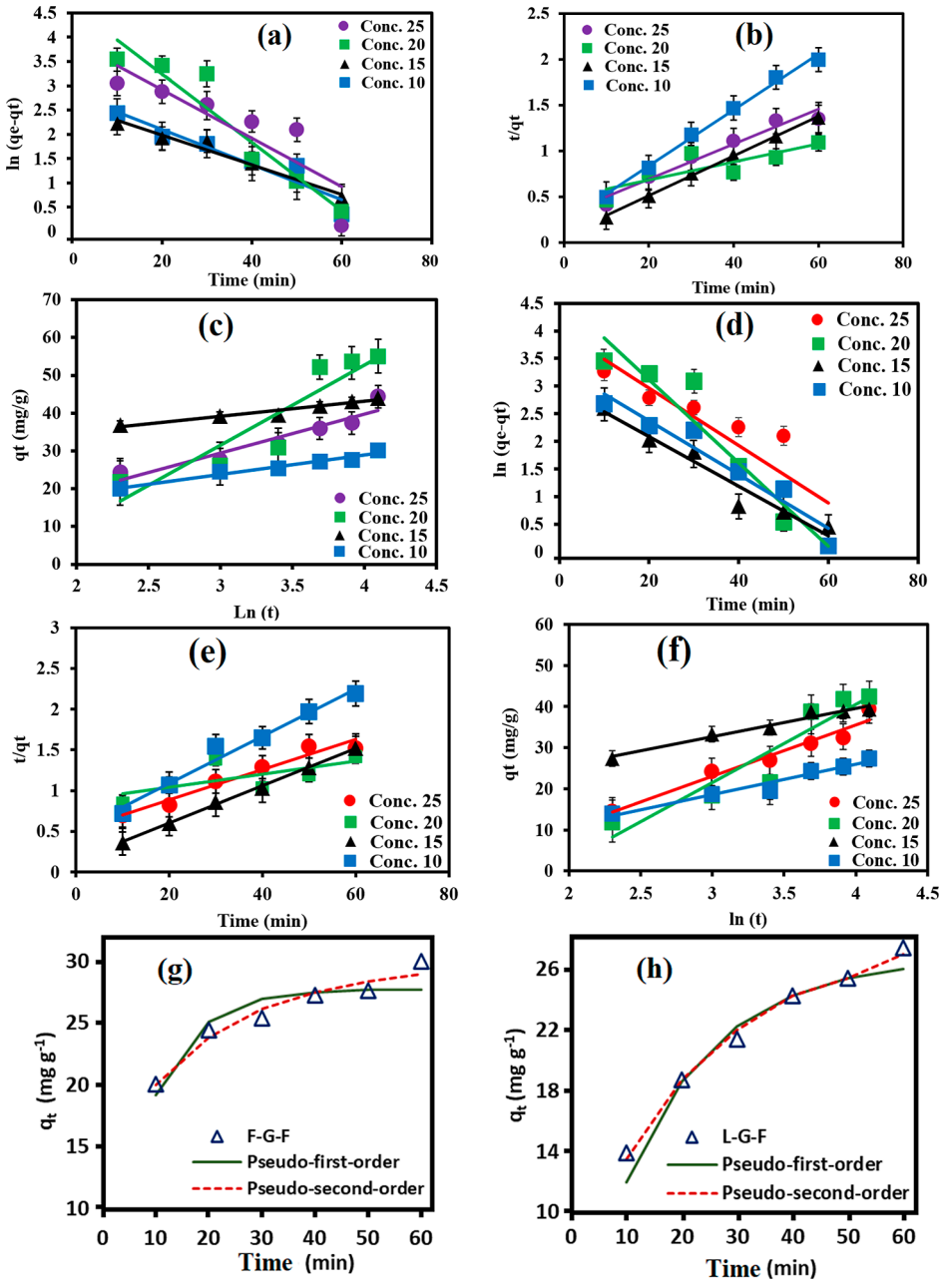

Figure 5. Linear fit of the pseudo first-order (a), pseudo second-order (b), and Elovich (c) kinetic model analyses of F-G-F and pseudo-first-order (d), pseudo-second-order (e), and Elovich (f) kinetic model analyses of L-G-F. Non-linear fit of pseudo-first-order and pseudo-second-order of F-G-F (g) and L-G-F (h).

75.49% after 60 min accompanied by an increase in the adsorption capacity from 45 to 56.6 mg/g. Comparing with F-G and L-G at the same conditions (Figure S6b), they show less removal percent than the ferrocene composite as F-G acquired 64.2 *R* %, while L-G managed 62.51% after 1 h. The adsorption capacity of F-G (48.2 mg/g) was slightly better than L-G (46.88 mg/g). The rapid removal obtained in the initial 30 min is attributed to the availability of many free active sites on the adsorbent material but after a period of time these sites become saturated and the free binding sites decrease in number, thus slowing the adsorption process afterward.[89] The same trend was observed when ferrihydrite (F), goethite (G), and magnetite were used in the removal of PO_4^{3-} from 100 mg L^{-1} solution, but the maximum adsorption capacity, 8.96 mg/g for F, 7.95 mg/g for M, and 7.16 mg/g for G, was achieved after 120 min.[90] The adsorbed amount of phosphate by magnetic diatomite and illite clay nanocomposites were 3.30 and 3.16 mg/g, respectively. The maximum removal also was in the first 30 min, and the further increase of contact time did not significantly affect the adsorption capacity.[91]

3.2.3. Effect of Adsorbent Dose. To better understand how the dose can affect the adsorption process, different doses in the range of 10−50 mg were utilized at an optimum experimental pH of 3, temperature = 25 °C, time = 60 min, and initial concentration = 15 mg L^{-1}. When graphene without ferrocene was used as an adsorbent material (Figure S6c), the *R* % of F-G increased from 63.17% at 0.01 g dosage to 76.39% at 0.05 g dose, while the adsorption capacity decreases from to 47.3 to 11.4 mg/g. L-G removal percentage was 74.8% with an adsorption capacity of 11.23 mg/g when 0.05 g dose was

https://doi.org/10.1021/acsomega.2c05985
ACS Omega 2022, 7, 45386−45402

Table 2. Linear Kinetic Parameters of F-G-F and L-G-F

	F-G-F			
	concentration (mg L^{-1})			
parameter	10	15	20	25
$q_{e,exp}$ (mg g^{-1})	39.5	58	57.2	55.7
	pseudo-first-order model			
$q_{e,cal}$ (mg g^{-1})	16.6	14.9	102.12	52.7
k_1 (min^{-1})	0.000702	0.00053	0.001272	0.00082
R^2	0.902	0.961	0.913	0.762
	pseudo-second-order model			
$q_{e,cal}$ (mg g^{-1})	34.72	47.3	100.1	46.4
k_2 (mg g^{-1})	0.004463	0.007188	0.000302	0.005085
R^2	0.994	0.997	0.761	0.954
	Elovich model			
β (g mg^{-1})	0.18	0.37	0.05	0.94
α (mg g min^{-1})	26.8051	3395.725	96.08053	0.09705
R^2	0.970	0.949	0.843	0.896
	L-G-F			
	concentration (mg L^{-1})			
parameter	10	15	20	25
$q_{e,exp}$ (mg g^{-1})	38.5	56.5	54.8	53.6
	pseudo-first-order model			
$q_{e,cal}$ (mg g^{-1})	30.27	20.19	101.37	54.71
k_1 (min^{-1})	0.000853	0.000754	0.001271	0.000836
R^2	0.924	0.946	0.921	0.794
	pseudo-second-order model			
$q_{e,cal}$ (mg g^{-1})	35.6	46.62	60.2	54.02
k_2 (mg g^{-1})	0.001725	0.00351	0.000287	0.00065
R^2	0.973	0.998	0.942	0.956
	Elovich model			
β (g mg^{-1})	0.14	0.15	0.06	0.08
α (mg g min^{-1})	4.80	38.58	2.97	3.98
R^2	0.953	0.967	0.881	0.95

implemented; however, when 0.01 g dose was used the removal of phosphate was 61.07% and the adsorption capacity became 45.8 mg/g. A chart of the adsorption capacity and removal percentage of the composite samples is shown in Figure 4c. The removal efficiency sharply increased when the dosage shifted from 0.01 to 0.03 g and then was gradually raised till it reached its maximum percent at 0.05 g dosage while the adsorption amount sharply declined. L-G-F depicted that as the adsorbent amount increased from 0.01 to 0.05 g, the removal efficiency increased from 75.49 to 80.6% while on the contrary, the adsorption capacity significantly dropped from 56.6 to 12 mg/g. F-G-F presented a relatively higher percent removal than L-G-F. The removal percentage was raised from nearly 78.5% at an adsorbent dose of 0.01 g to 83.67% at dose = 0.05 g, while the adsorption capacity decreased from 58.9 to 12.6 mg/g. The observed increase in the removal rate when the dose was increased may be attributed to the promotion of active sites on the adsorbent. However, the adsorption amount was its highest at the initial doses and then decreased by increasing the dose, which could be due to the complete interaction between the adsorbent material and the phosphate at small doses, and any increment in the dosage will provide more active sites than the available phosphate ions that need to be adsorbed. These extra active locations become not fully occupied by the adsorbate and the adsorption capacity falls dramatically.[4,92] Distiller grain biochar[93] and lanthanum-loaded carboxymethyl konjac glucomannan microspheres (CMKGM-La)[89] have also presented the same trend when the adsorbent amount was increased. From the perspective of economic costs and because it has presented good removal efficiency, 0.01 g dose was selected as the optimum subsequent experimental dosage.

3.2.4. Effect of Initial Concentration. The initial concentration of the phosphate solution strongly affected the adsorption process. In order to investigate the influence of the initial phosphate concentration, different concentrations from 5 to 25 mg L^{-1} were examined at room temperature, while other experimental parameters were kept at the optimal, examined, and chosen conditions of pH = 3, dose of 0.01 g, and contact time = 60 min. The adsorption capacity of the F-G-F (Figure 4d) rose significantly from 20.6 to 58 mg/g as the concentration increased from 5 to 15 mg L^{-1} and became almost stable, 57.24 and 55.71 mg/g, at higher concentrations of 20 and 25 mg L^{-1}, respectively. The removal efficiency sharply decreased from 82.4% at a concentration of 5 mg L^{-1} to 47% at a concentration of 25 mg L^{-1}, which could be attributed to the higher availability of active sites at lower concentrations that subjected phosphate ions to binding sites, while at higher concentrations these sites become saturated.[89] Moreover, at higher concentrations, the ratio between active binding sites and the initial concentration became low leading to a decrease in the removal rate.[49,94] L-G-F presented the same trend; however, it showed a relatively lower removal percentage of 79.1% at a concentration of 5 mg L^{-1}, while its

https://doi.org/10.1021/acsomega.2c05985
ACS Omega 2022, 7, 45386−45402

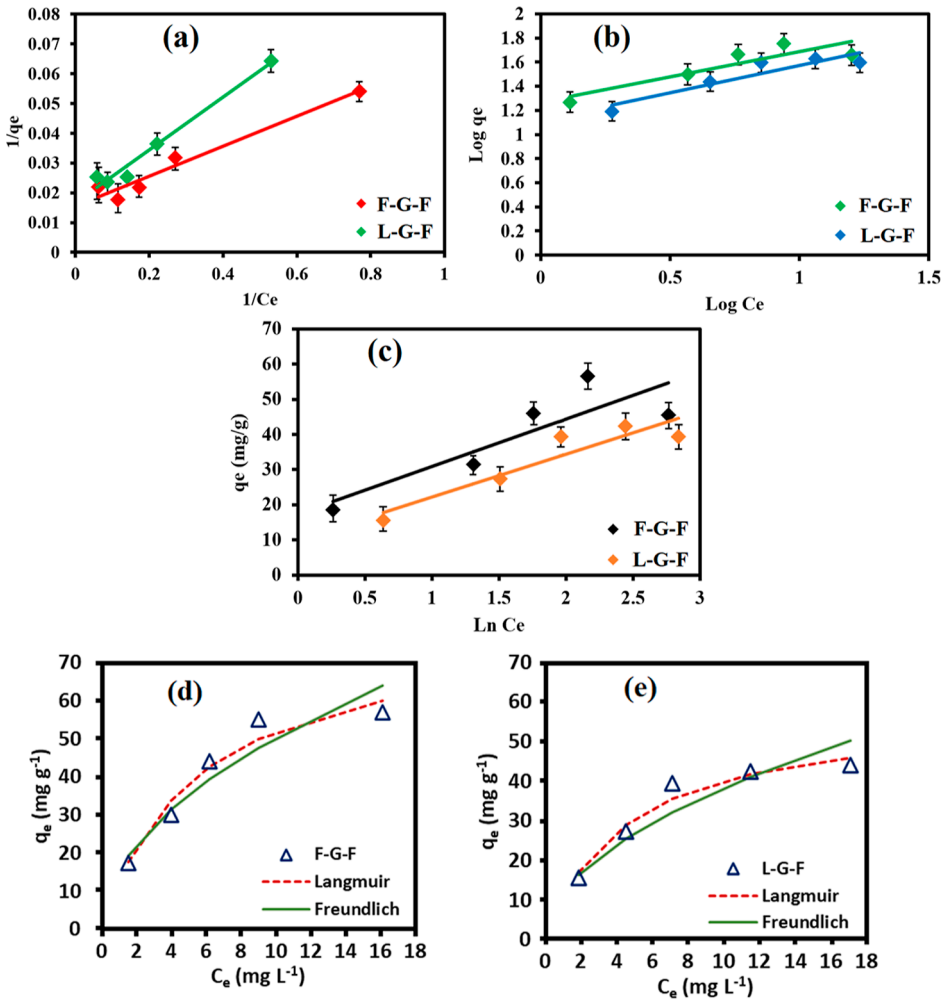

Figure 6. Linear fit of Langmuir (a), Freundlich (b), and Temkin (c) isotherm models of F-G-F and L-G-F. Non-linear fit of Langmuir and Freundlich isotherm models of F-G-F (d) and L-G-F (e).

higher adsorption capacity was 56.5 mg/g at a concentration of 15 mg L^{-1}. Although F-G and L-G show a similar trend with increasing the initial concentration of the phosphate solution (Figure S6d), they were less effective than the composites. F-G removal efficiency was 71.5% at C_i = 5 mg L^{-1} and decreased to 43.08% at C_i = 25 mg L^{-1}, while the adsorption capacity increased from 17.8 to 53.5 mg/g. L-G removal percent was 69.2% with an adsorption capacity of 17.3 mg/g at a phosphate concentration of 5 mg L^{-1} and when the concentration increased to 25 mg L^{-1}, the R % became 40.52 and the adsorption capacity increased to 50.65 mg/g. These outcomes are in line with many studies.[95,96]

3.2.5. Adsorption Kinetics. The adsorption rate of phosphate removal onto graphene synthesized by palm fibers and leaves was analyzed using the linear pseudo-first-order, pseudo-second-order, and Elovich kinetic models. The curves of fitting these models to the equilibrium data of different initial concentrations are shown in Figure 5a–f, while the results of the kinetic parameters are shown in Table 2.

The high R^2 values in the three models indicate that all can fit the adsorption process; nevertheless, the pseudo-second-order R^2 is the highest among all concentrations except 20 mg L^{-1} in F-G-F as the R^2 of the pseudo-first-order was higher. The calculated adsorption capacity $q_{e\ cal}$ of the pseudo-second-order is the closest to the experimental data in all initial concentrations; thus, the pseudo-second-order is the most suitable according to the higher R^2 and the good agreement between experimental and calculated q_e. The Elovich model cannot be used to describe this adsorption process because of the huge value of error between the calculated and experimental q_e values along with the least R^2 value compared to the other two models. It is observed that the higher value of α than β depicted a higher adsorption rate than desorption, which indicates that phosphate has a strong affinity to be adsorbed on the F-G-F and L-G-F surfaces.[97] The non-linear form of the pseudo-first-order and pseudo-second-order kinetic models has been also adopted in order to illustrate the adsorption process with more accurate variables and parameters (Table S3). The data collected from the influence of contact time has been used to calculate and plot the order and rate kinetic constants of PO_4^{3-} adsorption onto graphene. Figure 5g,h depicts the increase of phosphate uptake till equilibrium at 60 min. The removal capacity was high in the first 30 min due to the availability of many active sites on the graphene materials. The phosphate adsorption rate constant was fitted to the pseudo-second order (R^2 = 0.957 and 0.994 for F-G-F and L-G-F, respectively). The pseudo-second order supposes that the rate of adsorption is proportionate to the available sites on the adsorbent, which suggests that the adsorption process may be a chemisorption process.[98]

https://doi.org/10.1021/acsomega.2c05985
ACS Omega 2022, 7, 45386−45402

Table 3. Linear Isotherm Parameters of F-G-F and L-G-F

F-G-F	Langmuir			Freundlich			Temkin		
q_m mg g^{-1}	K_L L mg^{-1}	R_L	R^2	K_F L mg^{-1}	n	R^2	B_T J mol^{-1}	K_T L mg^{-1}	R^2
64.94	0.31	0.18	0.95	18.54	2.38	0.80	13.46	3.63	0.74
L-G-F	Langmuir			Freundlich			Temkin		
q_m mg g^{-1}	K_L L mg^{-1}	R_L	R^2	K_F L mg^{-1}	n	R^2	B_T J mol^{-1}	K_T L mg^{-1}	R^2
60.24	0.19	0.26	0.97	13.19	2.22	0.86	12.18	2.27	0.86

Table 4. Phosphate Adsorption Capacities Using Various Biomaterials in the Literature to Compare with the Recent Study

adsorbent material	synthesis method	pH	time (min)	adsorption capacity (mg/g)	refs
modified bentonites	stirring with metal salts	6.5	60	8.33	108
sewage sludge	chemical activation with pyrolusite	4	30	10.78	109
polyaniline/TiO_2 composite	chemical oxidative polymerization of aniline monomer	3	60	12.11	110
Al−NaBT−Ca−alginate	modification of bentonite	3	1440	15.8	111
iron-zirconium-modified activated carbon nanofiber	loading zirconium and iron particles on the surface of ACF	4	1440	26.3	112
dolomite-modified biochar	pyrolysis	4.5	120	29.18	113
Ti−GO composite	sole gel process	6	1440	33.11	114
goethite	chemical synthesis	6	120	50.5	90
graphene ferrocene composite	palm leaf carbonization	3	60	56.6	current study
graphene ferrocene composite	palm fiber carbonization	3	60	58.93	current study
α-Fe_2O_3−GO composite	ultrasonic treatment	6	5	93.28	107

3.2.6. Adsorption Isotherms. Modeling the adsorption data using isotherm models helps in better understanding the adsorption mechanism that can be either by chemical bond formation, ion exchange, or physical adsorption through van der Waals forces and also evaluate the performance of the adsorbent material by indicating maximum adsorption capacity.[99] The Langmuir, Freundlich, and Temkin linear models were adopted to illustrate the adsorption isotherm. The Langmuir model represents chemical adsorption and assumes that the adsorption process happens on a homogenous monolayer surface that requires similar adsorption energy for all active sites.[100] The Freundlich model represents the physical adsorption and presumes that the adsorption process takes place on a multilayer heterogeneous surface with different adsorption sites having different affinities,[101] while the Temkin model assumes that adsorption is a multi-layer process that considers the adsorbent−adsorbate interactions and the heat of adsorption of all molecules in the layer decreases linearly with the coverage.[102] The fitting of these adsorption isotherm models is shown in Figure 6a−c, and the isotherm parameters are shown in Table 3. R^2 values confirm that the Langmuir isotherm is the best fit for the adsorption of phosphate on both the F-G-F and L-G-F surfaces (0.957 and 0.976, respectively) as it is more close to unity than Freundlich (0.8015 and 0.857, respectively) and Temkin (0.741 and 0.860, respectively) models. Q_{max} obtained from the Langmuir was 64.9 and 60.24 mg/g for F-G-F and L-G-F, respectively, which is more or less close to the experimental q_e that was 58.9 mg/g for F-G-F and 56.6 mg/g for L-G-F, elucidating that the main adsorption occurred on the monolayer or through a definite number of identical locations on the F-G-F and L-G-F surfaces. In addition, the dimensionless separation factor (R_L) falls between 0 and 1 (0.17 and 0.26 for F-G-F and L-G-F, respectively) along with the n value (2.38 and 2.22 for F-G-F and L-G-F, respectively) calculated from the Freundlich model indicated that the phosphate adsorption onto the F-G-F and L-G-F was favorable as the n value is more than unity.[102] The values obtained from the Temkin isotherm for F-G-F were as follows: K_T = 3.6 L/mg and B_T = 13.62 J mol^{-1}, while for L-G-F the values were as follows: K_T = 2.26 L/mg and B_T = 12.17 J mol^{-1} because the value of b (intercept) = 17.354 and 9.96 for F-G-F and L-G-F, respectively, which is less than 80 KJ/mol; it is suggested that the adsorption of phosphate was via physisorption, in which the adsorbate is attached onto the adsorbent through the weak interactions of van der Waals and as a result relatively low adsorption energy is required.[103] The non-linear isotherm was investigated through the application of non-linear form of Langmuir and Freundlich models. The results are shown in Figure 6d,e, while the isotherm parameters are tabulated in Table S3. The R^2 obtained from the Langmuir model of both F-G-F and L-G-F was the highest and the q_m supposed that the maximum adsorption uptakes of PO_4^{3-} in homogenous monolayer are 80.51 and 58.17 mg g^{-1}, respectively. The K_L was 0.183 and 0.22 for F-G-F and L-G-F, respectively, which was much higher than many adsorbent materials such as lanthanum hydroxide[88] and CaO_2/biochar composite,[104] confirming the affinity of the synthesized graphene for PO_4^{3-}. Based on such findings, the Langmuir model adequately described the adsorption data. The results are in line with many previous studies including when phosphate was adsorbed onto zirconium-modified bentonite[105] and when phosphate-binding protein resin was implemented in phosphate removal.[106] The diagram in Figure S6 visualizes the experimental results' error by comparing the experimental adsorption capacity (q exp.) with the calculated adsorption capacity (q cal.) from adsorption models.

Comparing the adsorption capacity obtained by the current work with that presented in the relevant literature published in the last 6 years (Table 4) revealed that ours is higher except Bai et al.,[107] who used the α-Fe_2O_3−GO composite for

https://doi.org/10.1021/acsomega.2c05985
ACS Omega 2022, 7, 45386−45402

phosphate removal. Nevertheless, they used a harsh chemical method coupled with ultrasonication to synthesize the nanocomposite. In the current work, we adopted a green route for synthesizing graphene using readily available and cheap biomass to avoid using harmful chemicals for the sake of environmental conservation.

3.2.7. Regeneration Studies. The reusability of F-G-F and L-G-F was evaluated by the regeneration of phosphate-loaded adsorbent after the batch adsorption experiments. As presented in Figure 7, four consecutive adsorption/desorption cycles

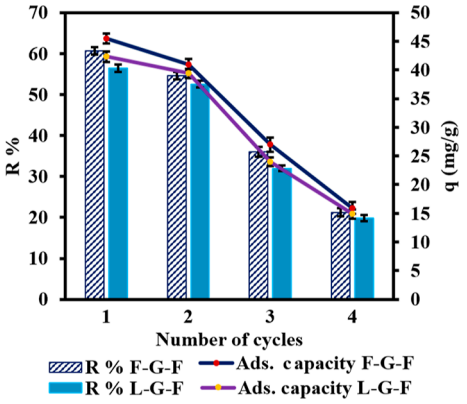

Figure 7. Reusability study of phosphate ion removal by the ferrocene-functionalized biographene.

were performed. The adsorption efficiency of F-G-F and L-G-F dropped from 60.67 and 56.44%, respectively, in the first regeneration cycle to 21.25 and 19.83%, respectively, in the fourth cycle. The adsorption capacity also decreased dramatically from 45.5 to 15.94 mg/g when F-G-F was used and from 42.33 to 14.8 mg/g using L-G-F. The reason behind this decrease may be due to incomplete desorption and loss of functional groups.[115,116] These results indicate that the synthesized biographene can be reusable for phosphate removal from water but within limited times. The results are still better than the Al_{30} polyoxocation−GO composite that showed no reusability potentials;[117] however, the cerium-reduced GO nanocomposite presented a very good stable removal efficiency of 95% after four adsorption−desorption cycles.[118]

3.2.8. Removal of Phosphate from Real Wastewater Samples. The potential of F-G-F in remediating real wastewater sample from phosphate pollution was examined by applying the best-examined conditions obtained from the batch adsorption experiments (pH: 3, F-G-F dose: 0.01 g, and temperature: 25 ± 2 °C). Although the composition of the real effluent wastewater is much more complicated than the artificial solutions prepared in the laboratory, phosphate was quickly adsorbed in the first 30 min of the adsorption process, as shown in Figure S8, and gradually removed till reaching equilibrium after 70 min. With increasing contact time, the removal efficiency improved from 45.22 to 75.09% and the adsorption capacity increased from 18.24 to 30.3 mg/g, which further confirmed the suitability of the synthesized graphene composite for phosphate removal from real wastewater. For the sake of comparison, F-G performance in the real wastewater sample was investigated. The removal efficiency was 67.7% and the adsorption capacity was 27.35 mg/g after a 70 min period which concluded that the ferrocene-functionalized graphene boosted the adsorption efficiency to a good extent. These results revealed that F-G-F is more efficient than many adsorbents, such as magnesium-modified biochar,[119] $La(OH)_3$−biochar hybrid,[120] and Al−biochar composite,[119] as they acquired lower removal potentials. However, imprinted polymers showed a close affinity for phosphate as F-G-F (75%).[121]

3.2.9. Adsorption Mechanism of Phosphate onto the Synthesized Biographene Surface. The adsorption of phosphate ions on the F-G-F and L-G-F surfaces, as shown in Figure 8, follows the ion exchange (chemical adsorption)

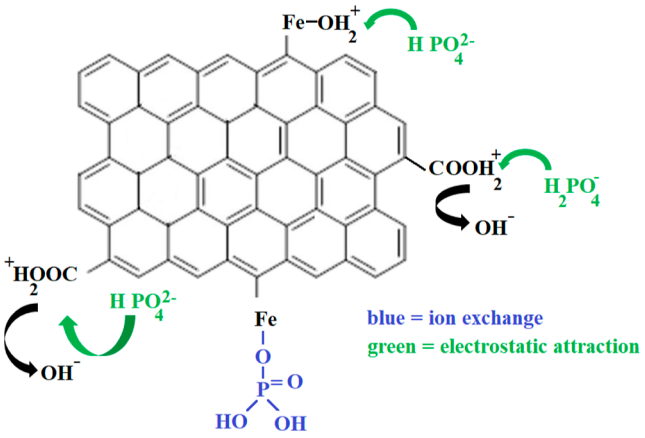

Figure 8. Adsorption mechanism of phosphate onto the biographene surface.

mechanisms, which was confirmed by the data obtained from the pH effect as increasing pH was associated with increasing hydroxyl ions that competed with the phosphate ions on the active sites of the graphene surface and decreased the removal percentage. This interpretation is also in line with the adsorption isotherm results as the adsorption process fits well with the Langmuir model. Furthermore, energy-dispersive X-ray spectroscopy (EDX) and XRD analyses confirmed the presence of iron on the surface of synthesized biographene that may be contributed to removing the negative phosphate ions by the electrostatic attraction between negative and positive ions.

4. CONCLUSIONS

Palm byproducts were used as a carbon source to synthesize ferrocene-functionalized graphene in an eco-friendly manner. The obtained composite acquired a sheet-like morphology as observed by SEM. The XRD pattern demonstrated the existence of the graphene characteristic peak related to the carbon $\pi-\pi$ interaction at 2 theta = 22°, while Raman D and G bands also confirmed the successful fabrication of high-quality graphene. Peaks illustrated by FTIR and UV emphasized the presence of active phytoconstituents in palm leaves and fibers. Furthermore, zeta potential analysis indicated the presence of negative charges on the graphene surface, which explained its stability and well-dispersed appearance. TGA results revealed that most of the resultant material degradation was in regions 2 and 3, confirming the formation of the desired graphene composite. The phosphate removal potential of F-G-F, 78.57%, was found to be relatively higher than that of L-G-F, 75.55%. The optimum examined conditions of the synthesized F-G-F that triggered this removal percent were after 1 h of contact time, pH = 3, dose = 0.01 g, and initial concentration = 15 mg

https://doi.org/10.1021/acsomega.2c05985
ACS Omega 2022, 7, 45386−45402

L^{-1}. The pseudo-second-order kinetic model and Langmuir isotherm were the best fit to describe the adsorption process, while the maximum uptake capacity was 58.9 mg/g for F-G-F and 56.6 mg/g for L-G-F. The synthesized graphene was efficient in phosphate removal from a real wastewater sample using the optimum examined conditions as it removed 75.09% of phosphate with an adsorption capacity of 30.03 mg g^{-1}.

■ ASSOCIATED CONTENT

Supporting Information

The Supporting Information is available free of charge at https://pubs.acs.org/doi/10.1021/acsomega.2c05985.

> Advantages and disadvantages of the pyrolysis methods; identification and quantification of the graphene functional groups by TGA analysis; non-linear kinetic and isotherm parameters; wastewater effluent characteristics; ferrocene structure; SEM image of palm leaves after pyrolysis with ferrocene at different magnifications; XRD patterns of the synthesized F-G-F and L-G-F; UV spectrum of ferrocene, plant extracts of palm leaves and fibers, L-G-F and F-G-F; FTIR spectra of palm leaves and palm fibers biomass, F-G, L-G, F-G-F, and L-G-F; zeta potential of L-G-F and F-G-F; EDX analysis of L-G-F, F-G-F, L-G, and F-G; homogenous dispersion of the produced biographene in water; Raman spectrum of GO, F-G-F, and L-G-F; PO_4^{3-} removal efficiency and adsorption capacity of the synthesized F-G and L-G using different pH, time, doses, and PO_4^{3-} concentrations; diagram representing the error between the experimental and calculated adsorption capacity using F-G-F and L-G-F at different phosphate concentrations; and performance of F-G-F and F-G in phosphate removal from real wastewater effluent sample (PDF)

■ AUTHOR INFORMATION

Corresponding Author

Nourhan El-Maghrabi − *Environmental Sciences Department, Faculty of Science, Alexandria University, Alexandria 21511, Egypt; Green Technology Group, Faculty of Science, Alexandria University, Alexandria 21511, Egypt;* orcid.org/0000-0001-6097-3208; Email: nourhanahmed2294@gmail.com, nourhan.elmaghrabi@alexu.edu.eg

Authors

Manal Fawzy − *Environmental Sciences Department, Faculty of Science, Alexandria University, Alexandria 21511, Egypt; Green Technology Group, Faculty of Science, Alexandria University, Alexandria 21511, Egypt; National Biotechnology Network of Expertise (NBNE), Academy of Scientific Research and Technology (ASRT), Cairo 11694, Egypt;* orcid.org/0000-0002-9401-9049

Alaa El Din Mahmoud − *Environmental Sciences Department, Faculty of Science, Alexandria University, Alexandria 21511, Egypt; Green Technology Group, Faculty of Science, Alexandria University, Alexandria 21511, Egypt;* orcid.org/0000-0001-6530-9816

Complete contact information is available at: https://pubs.acs.org/10.1021/acsomega.2c05985

Author Contributions

N.E.-M.: investigation, conceptualization, formal analysis, methodology, data curation, visualization, and writing the manuscript. M.F.: conceptualization, resources, funding acquisition, project administration, supervision, and reviewing the final manuscript. A.E.D.M.: supervision, conceptualization, project administration, resources, and reviewing the final manuscript.

Notes

The authors declare no competing financial interest.

■ ACKNOWLEDGMENTS

This research was supported by the Egyptian Science, Technology & Innovation Funding Authority (STDF), grant number 45888 under the umbrella of USAID/STDF collaborative project and the SA-Egypt Joint Project from the Egypt's Academy of Scientific Research and Technology (ASRT), grant number 7981.

■ REFERENCES

(1) Novais, S. V.; Zenero, M. D. O.; Barreto, M. S. C.; Montes, C. R.; Cerri, C. E. P. Phosphorus removal from eutrophic water using modified biochar. *Sci. Total Environ.* **2018**, *633*, 825−835.

(2) Wang, J.; Chen, J.; Jin, Z.; Guo, J.; Yang, H.; Zeng, Y.; Liu, Y. Simultaneous removal of phosphate and ammonium nitrogen from agricultural runoff by amending soil in lakeside zone of Karst area, Southern China. *Agric., Ecosyst. Environ.* **2020**, *289*, 106745.

(3) Yin, Q.; Wang, R.; Zhao, Z. Application of Mg−Al-modified biochar for simultaneous removal of ammonium, nitrate, and phosphate from eutrophic water. *J. Cleaner Prod.* **2018**, *176*, 230−240.

(4) Liu, F.; Yang, J.; Zuo, J.; Ma, D.; Gan, L.; Xie, B.; Wang, P.; Yang, B. Graphene-supported nanoscale zero-valent iron: removal of phosphorus from aqueous solution and mechanistic study. *J. Environ. Sci.* **2014**, *26*, 1751−1762.

(5) Oliver, R. L.; Ganf, G. G.Freshwater blooms. *The ecology of cyanobacteria*; Springer, 2000; pp 149−194.

(6) Lewis, W. M., Jr.; Wurtsbaugh, W. A.; Paerl, H. W. Rationale for control of anthropogenic nitrogen and phosphorus to reduce eutrophication of inland waters. *Environ. Sci. Technol.* **2011**, *45*, 10300−10305.

(7) Wang, Q.; Liao, Z.; Yao, D.; Yang, Z.; Wu, Y.; Tang, C. Phosphorus immobilization in water and sediment using iron-based materials: A review. *Sci. Total Environ.* **2021**, *767*, 144246.

(8) Yan, Y.; Nashath, F. Z.; Chen, S.; Manickam, S.; Lim, S. S.; Zhao, H.; Lester, E.; Wu, T.; Pang, C. H. Synthesis of graphene: Potential carbon precursors and approaches. *Nanotechnol. Rev.* **2020**, *9*, 1284−1314.

(9) Mohan, A. N.; Manoj, B. Extraction of graphene nanostructures from Colocasia esculenta and Nelumbo nucifera leaves and surface functionalization with tin oxide: Evaluation of their antibacterial properties. *Chem.—Eur. J.* **2020**, *26*, 8105−8114.

(10) Prekodravac, J. R.; Kepić, D. P.; Colmenares, J. C.; Giannakoudakis, D. A.; Jovanović, S. P. A comprehensive review on selected graphene synthesis methods: From electrochemical exfoliation through rapid thermal annealing towards biomass pyrolysis. *J. Mater. Chem. C* **2021**, *9*, 6722−6748.

(11) Zhang, Y.; Cui, Y.; Chen, P.; Liu, S.; Zhou, N.; Ding, K.; Fan, L.; Peng, P.; Min, M.; Cheng, Y.; Wang, Y.; Wan, Y.; Liu, Y.; Li, B.; Ruan, R.Chapter 14—Gasification Technologies and Their Energy Potentials. *Sustainable Resource Recovery and Zero Waste Approaches*; Taherzadeh, M. J., Bolton, K., Wong, J., Pandey, A., Eds.; Elsevier, 2019; pp 193−206.

(12) Hosny, M.; Fawzy, M.; Eltaweil, A. S. Green synthesis of bimetallic Ag/ZnO@Biohar nanocomposite for photocatalytic degradation of tetracycline, antibacterial and antioxidant activities. *Sci. Rep.* **2022**, *12*, 7316.

(13) Kong, X.; Zhu, Y.; Lei, H.; Wang, C.; Zhao, Y.; Huo, E.; Lin, X.; Zhang, Q.; Qian, M.; Mateo, W.; Zou, R.; Fang, Z.; Ruan, R. Synthesis of graphene-like carbon from biomass pyrolysis and its applications. *Chem. Eng. J.* **2020**, *399*, 125808.
(14) Sun, L.; Tian, C.; Li, M.; Meng, X.; Wang, L.; Wang, R.; Yin, J.; Fu, H. From coconut shell to porous graphene-like nanosheets for high-power supercapacitors. *J. Mater. Chem. A* **2013**, *1*, 6462−6470.
(15) Primo, A.; Atienzar, P.; Sanchez, E.; Delgado, J. M.; García, H. From biomass wastes to large-area, high-quality, N-doped graphene: catalyst-free carbonization of chitosan coatings on arbitrary substrates. *Chem. Commun.* **2012**, *48*, 9254−9256.
(16) Suryawanshi, A.; Biswal, M.; Mhamane, D.; Gokhale, R.; Patil, S.; Guin, D.; Ogale, S. Large scale synthesis of graphene quantum dots (GQDs) from waste biomass and their use as an efficient and selective photoluminescence on−off−on probe for Ag+ ions. *Nanoscale* **2014**, *6*, 11664−11670.
(17) Du, Q.-S.; Li, D.-P.; Long, S.-Y.; Tang, P.-D.; Du, F.-L.; Huang, H.-L.; Dai, J.; Xie, N.-Z.; Wang, Q.-Y.; Huang, R.-B. Graphene like porous carbon with wood-ear architecture prepared from specially pretreated lignin precursor. *Diamond Relat. Mater.* **2018**, *90*, 109−115.
(18) Hosny, M.; Fawzy, M.; Eltaweil, A. S. Phytofabrication of bimetallic silver-copper/biochar nanocomposite for environmental and medical applications. *J. Environ. Manage.* **2022**, *316*, 115238.
(19) Gao, K.; Niu, Q.; Tang, Q.; Guo, Y.; Wang, L. Graphene-like 2D porous carbon nanosheets derived from cornstalk pith for energy storage materials. *J. Electron. Mater.* **2018**, *47*, 337−346.
(20) Bhat, V. S.; Kanagavalli, P.; Sriram, G.; B, R. P.; John, N. S.; Veerapandian, M.; Kurkuri, M.; Hegde, G. Low cost, catalyst free, high performance supercapacitors based on porous nano carbon derived from agriculture waste. *J. Energy Storage* **2020**, *32*, 101829.
(21) Ali, G. A. M.; Habeeb, O. A.; Algarni, H.; Chong, K. F. CaO impregnated highly porous honeycomb activated carbon from agriculture waste: symmetrical supercapacitor study. *J. Mater. Sci.* **2019**, *54*, 683−692.
(22) Eltaweil, A. S.; Abdelfatah, A. M.; Hosny, M.; Fawzy, M. Novel Biogenic Synthesis of a Ag@Biochar Nanocomposite as an Antimicrobial Agent and Photocatalyst for Methylene Blue Degradation. *ACS Omega* **2022**, *7*, 8046−8059.
(23) Om Prakash, M.; Raghavendra, G.; Ojha, S.; Panchal, M. Characterization of porous activated carbon prepared from arhar stalks by single step chemical activation method. *Mater. Today: Proc.* **2021**, *39*, 1476−1481.
(24) Li, Z.; Wang, Q.; Zhou, Z.; Zhao, S.; Zhong, S.; Xu, L.; Gao, Y.; Cui, X. Green synthesis of carbon quantum dots from corn stalk shell by hydrothermal approach in near-critical water and applications in detecting and bioimaging. *Microchem. J.* **2021**, *166*, 106250.
(25) Moon, I. K.; Lee, J.; Ruoff, R. S.; Lee, H. Reduced graphene oxide by chemical graphitization. *Nat. Commun.* **2010**, *1*, 73.
(26) Lu, S. Y.; Jin, M.; Zhang, Y.; Niu, Y. B.; Gao, J. C.; Li, C. M. Chemically Exfoliating Biomass into a Graphene-like Porous Active Carbon with Rational Pore Structure, Good Conductivity, and Large Surface Area for High-Performance Supercapacitors. *Adv. Energy Mater.* **2018**, *8*, 1702545.
(27) Niu, J.; Shao, R.; Liu, M.; Zan, Y.; Dou, M.; Liu, J.; Zhang, Z.; Huang, Y.; Wang, F. Porous Carbons Derived from Collagen-Enriched Biomass: Tailored Design, Synthesis, and Application in Electrochemical Energy Storage and Conversion. *Adv. Funct. Mater.* **2019**, *29*, 1905095.
(28) Zhou, H.; Zhang, J.; Amiinu, I. S.; Zhang, C.; Liu, X.; Tu, W.; Pan, M.; Mu, S. Transforming waste biomass with an intrinsically porous network structure into porous nitrogen-doped graphene for highly efficient oxygen reduction. *Phys. Chem. Chem. Phys.* **2016**, *18*, 10392−10399.
(29) Baccile, N.; Laurent, G.; Babonneau, F.; Fayon, F.; Titirici, M.-M.; Antonietti, M. Structural characterization of hydrothermal carbon spheres by advanced solid-state MAS 13C NMR investigations. *J. Phys. Chem. C* **2009**, *113*, 9644−9654.
(30) Jiang, X.-F.; Wang, X.-B.; Dai, P.; Li, X.; Weng, Q.; Wang, X.; Tang, D.-M.; Tang, J.; Bando, Y.; Golberg, D. High-throughput fabrication of strutted graphene by ammonium-assisted chemical blowing for high-performance supercapacitors. *Nano Energy* **2015**, *16*, 81−90.
(31) Wang, J.; Kaskel, S. KOH activation of carbon-based materials for energy storage. *J. Mater. Chem. A* **2012**, *22*, 23710−23725.
(32) Visconti, P.; Primiceri, P.; Longo, D.; Strafella, L.; Carlucci, A. P.; Lomascolo, M.; Cretì, A.; Mele, G. Photo-ignition process of multiwall carbon nanotubes and ferrocene by continuous wave Xe lamp illumination. *Beilstein J. Nanotechnol.* **2017**, *8*, 134−144.
(33) Bhatt, V.Chapter 7—Basic Organometallic Chemistry. *Essentials of Coordination Chemistry*; Bhatt, V., Ed.; Academic Press, 2016; pp 173−190.
(34) Teimuri-Mofrad, R.; Hadi, R.; Abbasi, H. Synthesis and characterization of ferrocene-functionalized reduced graphene oxide nanocomposite as a supercapacitor electrode material. *J. Organomet. Chem.* **2019**, *880*, 355−362.
(35) Ashwin Karthick, N.; Thangappan, R.; Arivanandhan, M.; Gnanamani, A.; Jayavel, R. A facile synthesis of ferrocene functionalized graphene oxide nanocomposite for electrochemical sensing of lead. *J. Inorg. Organomet. Polym. Mater.* **2018**, *28*, 1021−1028.
(36) Tamilselvi, R.; Ramesh, M.; Lekshmi, G. S.; Bazaka, O.; Levchenko, I.; Bazaka, K.; Mandhakini, M. Graphene oxide-Based supercapacitors from agricultural wastes: A step to mass production of highly efficient electrodes for electrical transportation systems. *Renewable Energy* **2020**, *151*, 731−739.
(37) Rashid, R.; Shafiq, I.; Akhter, P.; Iqbal, M. J.; Hussain, M. A state-of-the-art review on wastewater treatment techniques: the effectiveness of adsorption method. *Environ. Sci. Pollut. Res.* **2021**, *28*, 9050−9066.
(38) Bacelo, H.; Pintor, A. M. A.; Santos, S. C. R.; Boaventura, R. A. R.; Botelho, C. M. S. Performance and prospects of different adsorbents for phosphorus uptake and recovery from water. *Chem. Eng. J.* **2020**, *381*, 122566.
(39) Jun, T.-S.; Park, N.-H.; So, D.-S.; Lee, J.-W.; Shim, K. B.; Ham, H. Phosphate removing by graphene oxide in aqueous solution. *J. Korean Cryst. Growth Cryst. Technol.* **2013**, *23*, 325−328.
(40) Koo, C. H.; Lau, W. J.; Lai, G. S.; Lai, S. O.; Thiam, H. S.; Ismail, A. F. Thin-Film Nanocomposite Nanofiltration Membranes Incorporated with Graphene Oxide for Phosphorus Removal. *Chem. Eng. Technol.* **2018**, *41*, 319−326.
(41) Liu, R.; Chi, L.; Wang, X.; Sui, Y.; Wang, Y.; Arandiyan, H. Review of metal (hydr)oxide and other adsorptive materials for phosphate removal from water. *J. Environ. Chem. Eng.* **2018**, *6*, 5269−5286.
(42) Ali, I.; Basheer, A. A.; Mbianda, X. Y.; Burakov, A.; Galunin, E.; Burakova, I.; Mkrtchyan, E.; Tkachev, A.; Grachev, V. Graphene based adsorbents for remediation of noxious pollutants from wastewater. *Environ. Int.* **2019**, *127*, 160−180.
(43) Yin, P. T.; Shah, S.; Chhowalla, M.; Lee, K.-B. Design, Synthesis, and Characterization of Graphene−Nanoparticle Hybrid Materials for Bioapplications. *Chem. Rev.* **2015**, *115*, 2483−2531.
(44) Othman, A.; Dumitrescu, E.; Andreescu, D.; Andreescu, S. Nanoporous Sorbents for the Removal and Recovery of Phosphorus from Eutrophic Waters: Sustainability Challenges and Solutions. *ACS Sustainable Chem. Eng.* **2018**, *6*, 12542−12561.
(45) Li, X.; Zhao, Y.; Wu, W.; Chen, J.; Chu, G.; Zou, H. Synthesis and characterizations of graphene−copper nanocomposites and their antifriction application. *J. Ind. Eng. Chem.* **2014**, *20*, 2043−2049.
(46) El-Maghrabi, N.; El-Borady, O. M.; Hosny, M.; Fawzy, M. Catalytic and Medical Potential of a Phyto-Functionalized Reduced Graphene Oxide−Gold Nanocomposite Using Willow-Leaved Knotgrass. *ACS Omega* **2021**, *6*, 34954−34966.
(47) Sateanchok, S.; Pankratova, N.; Cuartero, M.; Cherubini, T.; Grudpan, K.; Bakker, E. In-Line Seawater Phosphate Detection with Ion-Exchange Membrane Reagent Delivery. *ACS Sens.* **2018**, *3*, 2455−2462.

https://doi.org/10.1021/acsomega.2c05985
ACS Omega 2022, 7, 45386−45402

(48) Mahmoud, A. E. D.; El-Maghrabi, N.; Hosny, M.; Fawzy, M. Biogenic synthesis of reduced graphene oxide from Ziziphus spina-christi (Christ's thorn jujube) extracts for catalytic, antimicrobial, and antioxidant potentialities. *Environ. Sci. Pollut. Res.* **2022**, *29*, 89772−89787.
(49) Mahmoud, A. E. D.; Hosny, M.; El-Maghrabi, N.; Fawzy, M. Facile synthesis of reduced graphene oxide by Tecoma stans extracts for efficient removal of Ni (II) from water: batch experiments and response surface methodology. *Sustainable Environ. Res.* **2022**, *32*, 22.
(50) Kang, J.-K.; Seo, E.-J.; Lee, C.-G.; Park, S.-J. Fe-loaded biochar obtained from food waste for enhanced phosphate adsorption and its adsorption mechanism study via spectroscopic and experimental approach. *J. Environ. Chem. Eng.* **2021**, *9*, 105751.
(51) Shams, S. S.; Zhang, L. S.; Hu, R.; Zhang, R.; Zhu, J. Synthesis of graphene from biomass: a green chemistry approach. *Mater. Lett.* **2015**, *161*, 476−479.
(52) Rabti, A.; Mayorga-Martinez, C. C.; Baptista-Pires, L.; Raouafi, N.; Merkoçi, A. Ferrocene-functionalized graphene electrode for biosensing applications. *Anal. Chim. Acta* **2016**, *926*, 28−35.
(53) Niu, X.; Mo, Z.; Yang, X.; Shuai, C.; Liu, N.; Guo, R. Graphene-ferrocene functionalized cyclodextrin composite with high electrochemical recognition capability for phenylalanine enantiomers. *Bioelectrochemistry* **2019**, *128*, 74−82.
(54) Chen, F.; Yang, J.; Bai, T.; Long, B.; Zhou, X. Facile synthesis of few-layer graphene from biomass waste and its application in lithium ion batteries. *J. Electroanal. Chem.* **2016**, *768*, 18−26.
(55) Yuan, S.-J.; Dong, B.; Dai, X.-H. Facile and scalable synthesis of high-quality few-layer graphene from biomass by a universal solvent-free approach. *Appl. Surf. Sci.* **2021**, *562*, 150203.
(56) Chhetri, S.; Adak, N. C.; Samanta, P.; Murmu, N. C.; Hui, D.; Kuila, T.; Lee, J. H. Investigation of the mechanical and thermal properties of l-glutathione modified graphene/epoxy composites. *Composites, Part B* **2018**, *143*, 105−112.
(57) Baskakov, A. O.; Lyubutin, I. S.; Starchikov, S. S.; Davydov, V. A.; Kulikova, L. F.; Egorova, T. B.; Agafonov, V. N. Mechanism of transformation of ferrocene into carbon-encapsulated iron carbide nanoparticles at high pressures and temperatures. *Inorg. Chem.* **2018**, *57*, 14895−14903.
(58) Cruz, M. G. A.; de Oliveira, A. P. S.; Fernandes, F. A. N.; de Sousa, F. F.; Oliveira, A. C.; Filho, J. M.; Campos, A. F.; Rodríguez-Castellón, E. Fe-containing carbon obtained from ferrocene: Influence of the preparation procedure on the catalytic performance in FTS reaction. *Chem. Eng. J.* **2017**, *317*, 143−156.
(59) Dhivya, S.; Kalaichelvi, K. Screening of phytoconstituents, UV-VIS Spectrum and FTIR analysis of Micrococca mercurialis (L.) Benth. *Int. J. Tradit. Herb. Med.* **2017**, *5*, 40−44.
(60) Altaf, A. A.; Lal, B.; Badshah, A.; Usman, M.; Chatterjee, P. B.; Huq, F.; Ullah, S.; Crans, D. C. Synthesis, structural characterization, modal membrane interaction and anti-tumor cell line studies of nitrophenyl ferrocenes. *J. Mol. Struct.* **2016**, *1113*, 162−170.
(61) Ghayempour, S.; Montazer, M.; Mahmoudi Rad, M. M. Simultaneous encapsulation and stabilization of Aloe vera extract on cotton fabric for wound dressing application. *RSC Adv.* **2016**, *6*, 111895−111902.
(62) Nasrollahzadeh, M.; Atarod, M.; Sajadi, S. M. Green synthesis of the Cu/Fe3O4 nanoparticles using Morinda morindoides leaf aqueous extract: A highly efficient magnetically separable catalyst for the reduction of organic dyes in aqueous medium at room temperature. *Appl. Surf. Sci.* **2016**, *364*, 636−644.
(63) Tamilselvi, R.; Ramesh, M.; Lekshmi, G.; Bazaka, O.; Levchenko, I.; Bazaka, K.; Mandhakini, M. Graphene oxide−Based supercapacitors from agricultural wastes: A step to mass production of highly efficient electrodes for electrical transportation systems. *Renewable Energy* **2020**, *151*, 731−739.
(64) Li, G.; Zeng, J.; Zhao, L.; Wang, Z.; Dong, C.; Liang, J.; Zhou, Z.; Huang, Y. Amperometric cholesterol biosensor based on reduction graphene oxide-chitosan-ferrocene/platinum nanoparticles modified screen-printed electrode. *J. Nanopart. Res.* **2019**, *21*, 162.
(65) Li, C.; Qiu, X.; Deng, K.; Hou, Z. Electrochemical co-reduction synthesis of Au/ferrocene−graphene nanocomposites and their application in an electrochemical immunosensor of a breast cancer biomarker. *Anal. Methods* **2014**, *6*, 9078−9084.
(66) Liu, M.; Wang, L.; Deng, J.; Chen, Q.; Li, Y.; Zhang, Y.; Li, H.; Yao, S. Highly sensitive and selective dopamine biosensor based on a phenylethynyl ferrocene/graphene nanocomposite modified electrode. *Analyst* **2012**, *137*, 4577−4583.
(67) Patle, T. K.; Shrivas, K.; Kurrey, R.; Upadhyay, S.; Jangde, R.; Chauhan, R. Phytochemical screening and determination of phenolics and flavonoids in Dillenia pentagyna using UV−vis and FTIR spectroscopy. *Spectrochim. Acta, Part A* **2020**, *242*, 118717.
(68) Aragaw, B. A. Reduced graphene oxide-intercalated graphene oxide nano-hybrid for enhanced photoelectrochemical water reduction. *J. Nanostruct. Chem.* **2020**, *10*, 9−18.
(69) Wang, L.; Liu, M.; Meng, Y.; Li, H.; Zhang, Y.; Yao, S. (4-Ferrocenylethyne) phenylamine on Graphene as the Signal Amplificator to Determinate Dopamine and Acetaminophen Simultaneously. *Chin. J. Chem.* **2013**, *31*, 845−854.
(70) Papanikolaou, I.; Ribeiro de Souza, L.; Litina, C.; Al-Tabbaa, A. Investigation of the dispersion of multi-layer graphene nanoplatelets in cement composites using different superplasticiser treatments. *Constr. Build. Mater.* **2021**, *293*, 123543.
(71) Farivar, F.; Yap, P. L.; Hassan, K.; Tung, T. T.; Tran, D. N.; Pollard, A. J.; Losic, D. Unlocking thermogravimetric analysis (TGA) in the fight against "Fake graphene" materials. *Carbon* **2021**, *179*, 505−513.
(72) Zhou, Y.; Kandel, N.; Bartoli, M.; Serafim, L. F.; ElMetwally, A. E.; Falkenberg, S. M.; Paredes, X. E.; Nelson, C. J.; Smith, N.; Padovano, E.; Zhang, W.; Mintz, K. J.; Ferreira, B. C. L. B.; Cilingir, E. K.; Chen, J.; Shah, S. K.; Prabhakar, R.; Tagliaferro, A.; Wang, C.; Leblanc, R. M. Structure-activity relationship of carbon nitride dots in inhibiting Tau aggregation. *Carbon* **2022**, *193*, 1−16.
(73) Mintz, K. J.; Bartoli, M.; Rovere, M.; Zhou, Y.; Hettiarachchi, S. D.; Paudyal, S.; Chen, J.; Domena, J. B.; Liyanage, P. Y.; Sampson, R.; Khadka, D.; Pandey, R. R.; Huang, S.; Chusuei, C. C.; Tagliaferro, A.; Leblanc, R. M. A deep investigation into the structure of carbon dots. *Carbon* **2021**, *173*, 433−447.
(74) Tao, Y.; Li, S.; Li, P.; Wu, Q. Thermogravimetric analyses (TGA) of lignins isolated from the residue of corn stover bioethanol (CSB) production. *Holzforschung* **2016**, *70*, 1175−1182.
(75) Ruan, G.; Sun, Z.; Peng, Z.; Tour, J. M. Growth of graphene from food, insects, and waste. *ACS Nano* **2011**, *5*, 7601−7607.
(76) Ray, A. K.; Sahu, R. K.; Rajinikanth, V.; Bapari, H.; Ghosh, M.; Paul, P. Preparation and characterization of graphene and Ni-decorated graphene using flower petals as the precursor material. *Carbon* **2012**, *50*, 4123−4129.
(77) Borenstein, A.; Strauss, V.; Kowal, M. D.; Yoonessi, M.; Muni, M.; Anderson, M.; Kaner, R. B. Laser-reduced graphene-oxide/ferrocene: a 3-D redox-active composite for supercapacitor electrodes. *J. Mater. Chem. A* **2018**, *6*, 20463−20472.
(78) Sharma, N.; Sharma, V.; Vyas, R.; Kumari, M.; Kaushal, A.; Gupta, R.; Sharma, S. K.; Sachdev, K. A new sustainable green protocol for production of reduced graphene oxide and its gas sensing properties. *J. Sci.: Adv. Mater. Devices* **2019**, *4*, 473−482.
(79) Vázquez-Sánchez, P.; Rodríguez-Escudero, M. A.; Burgos, F. J.; Llorente, I.; Caballero-Calero, O.; González, M. M.; Fernández, R.; García-Alonso, M. C. Synthesis of Cu/rGO composites by chemical and thermal reduction of graphene oxide. *J. Alloys Compd.* **2019**, *800*, 0925−8388.
(80) Hou, D.; Liu, Q.; Wang, X.; Quan, Y.; Qiao, Z.; Yu, L.; Ding, S. Facile synthesis of graphene via reduction of graphene oxide by artemisinin in ethanol. *J. Materiomics* **2018**, *4*, 256−265.
(81) Ahmad, S.; Ahmad, A.; Khan, S.; Ahmad, S.; Khan, I.; Zada, S.; Fu, P. Algal extracts based biogenic synthesis of reduced graphene oxides (rGO) with enhanced heavy metals adsorption capability. *J. Ind. Eng. Chem.* **2019**, *72*, 117−124.
(82) Zhang, M.; Zhao, F.; Wang, Y.; Chen, X.; Pei, Q.; Xu, H.; Hao, H.; Yang, Y.; Li, H. Evaluation of graphene-ferrocene nanocomposite

https://doi.org/10.1021/acsomega.2c05985
ACS Omega 2022, 7, 45386−45402

as multifunctional combustion catalyst in AP-HTPB propellant. *Fuel* **2021**, *302*, 121229.
(83) Gu, Y.; Yang, M.; Wang, W.; Han, R. Phosphate adsorption from solution by zirconium-loaded carbon nanotubes in batch mode. *J. Chem. Eng. Data* **2019**, *64*, 2849−2858.
(84) Jung, K.-W.; Lee, S.; Lee, Y. J. Synthesis of novel magnesium ferrite (MgFe2O4)/biochar magnetic composites and its adsorption behavior for phosphate in aqueous solutions. *Bioresour. Technol.* **2017**, *245*, 751−759.
(85) Zhan, Y.; Zhang, H.; Lin, J.; Zhang, Z.; Gao, J. Role of zeolite's exchangeable cations in phosphate adsorption onto zirconium-modified zeolite. *J. Mol. Liq.* **2017**, *243*, 624−637.
(86) Qiu, B.; Duan, F. Synthesis of industrial solid wastes/biochar composites and their use for adsorption of phosphate: From surface properties to sorption mechanism. *Colloids Surf., A* **2019**, *571*, 86−93.
(87) Arshadi, M.; Abdolmaleki, M.; Eskandarloo, H.; Azizi, M.; Abbaspourrad, A. Synthesis of highly monodispersed, stable, and spherical NZVI of 20−30 nm on filter paper for the removal of phosphate from wastewater: batch and column study. *ACS Sustainable Chem. Eng.* **2018**, *6*, 11662−11676.
(88) Zhang, L.; Liu, Y.; Wang, Y.; Li, X.; Wang, Y. Investigation of phosphate removal mechanisms by a lanthanum hydroxide adsorbent using p-XRD, FTIR and XPS. *Appl. Surf. Sci.* **2021**, *557*, 149838.
(89) Zhang, X.; Lin, X.; He, Y.; Chen, Y.; Zhou, J.; Luo, X. Adsorption of phosphorus from slaughterhouse wastewater by carboxymethyl konjac glucomannan loaded with lanthanum. *Int. J. Biol. Macromol.* **2018**, *119*, 105−115.
(90) Ajmal, Z.; Muhmood, A.; Usman, M.; Kizito, S.; Lu, J.; Dong, R.; Wu, S. Phosphate removal from aqueous solution using iron oxides: Adsorption, desorption and regeneration characteristics. *J. Colloid Interface Sci.* **2018**, *528*, 145−155.
(91) Chen, J.; Yan, L.-g.; Yu, H.-q.; Li, S.; Qin, L.-l.; Liu, G.-q.; Li, Y.-f.; Du, B. Efficient removal of phosphate by facile prepared magnetic diatomite and illite clay from aqueous solution. *Chem. Eng. J.* **2016**, *287*, 162−172.
(92) Yoon, S.-Y.; Lee, C.-G.; Park, J.-A.; Kim, J.-H.; Kim, S.-B.; Lee, S.-H.; Choi, J.-W. Kinetic, equilibrium and thermodynamic studies for phosphate adsorption to magnetic iron oxide nanoparticles. *Chem. Eng. J.* **2014**, *236*, 341−347.
(93) Wang, B.; Lian, G.; Lee, X.; Gao, B.; Li, L.; Liu, T.; Zhang, X.; Zheng, Y. Phosphogypsum as a novel modifier for distillers grains biochar removal of phosphate from water. *Chemosphere* **2020**, *238*, 124684.
(94) Akram, M.; Bhatti, H. N.; Iqbal, M.; Noreen, S.; Sadaf, S. Biocomposite efficiency for Cr (VI) adsorption: Kinetic, equilibrium and thermodynamics studies. *J. Environ. Chem. Eng.* **2017**, *5*, 400−411.
(95) Trinh, V. T.; Pham, T. T. H.; Van, H. T.; Trinh, M. V.; Thang, P. Q.; Vu, X. H.; Nguyen, V. Q.; Dang, T. T. Phosphorus removal from aqueous solution by adsorption using silver nanoparticles: Batch experiment. *J. Hazard., Toxic Radioact. Waste* **2020**, *24*, 04020038.
(96) Trinh, V. T.; Nguyen, T. M. P.; Van, H. T.; Hoang, L. P.; Nguyen, T. V.; Ha, L.; Vu, X. H.; Pham, T.; Nguyen, T. N.; Quang, N.; Nguyen, X. C. Phosphate adsorption by silver nanoparticles-loaded activated carbon derived from tea residue. *Sci. Rep.* **2020**, *10*, 3634.
(97) Ahamad, K. U.; Singh, R.; Baruah, I.; Choudhury, H.; Sharma, M. R. Equilibrium and kinetics modeling of fluoride adsorption onto activated alumina, alum and brick powder. *Groundw. Sustain. Dev.* **2018**, *7*, 452−458.
(98) Zou, Y.; Zhang, R.; Wang, L.; Xue, K.; Chen, J. Strong adsorption of phosphate from aqueous solution by zirconium-loaded Ca-montmorillonite. *Appl. Clay Sci.* **2020**, *192*, 105638.
(99) Wang, J.; Guo, X. Adsorption isotherm models: Classification, physical meaning, application and solving method. *Chemosphere* **2020**, *258*, 127279.
(100) Langmuir, I. The adsorption of gases on plane surfaces of glass, mica and platinum. *J. Am. Chem. Soc.* **1918**, *40*, 1361−1403.
(101) Zhou, X.; Liu, Y.; Zhou, J.; Guo, J.; Ren, J.; Zhou, F. Efficient removal of lead from aqueous solution by urea-functionalized magnetic biochar: Preparation, characterization and mechanism study. *J. Taiwan Inst. Chem. Eng.* **2018**, *91*, 457−467.
(102) Araújo, C. S. T.; Almeida, I. L. S.; Rezende, H. C.; Marcionilio, S. M. L. O.; Léon, J. J. L.; de Matos, T. N. Elucidation of mechanism involved in adsorption of Pb(II) onto lobeira fruit (Solanum lycocarpum) using Langmuir, Freundlich and Temkin isotherms. *Microchem. J.* **2018**, *137*, 348−354.
(103) Et, A.; Shahmohammadi-Kalalagh, S. Isotherm and kinetic studies on adsorption of Pb, Zn and Cu by kaolinite. *Casp. J. Environ. Sci.* **2011**, *9*, 243−255.
(104) Li, X.; Xie, Y.; Jiang, F.; Wang, B.; Hu, Q.; Tang, Y.; Luo, T.; Wu, T. Enhanced phosphate removal from aqueous solution using resourceable nano-CaO2/BC composite: Behaviors and mechanisms. *Sci. Total Environ.* **2020**, *709*, 136123.
(105) Lin, J.; Jiang, B.; Zhan, Y. Effect of pre-treatment of bentonite with sodium and calcium ions on phosphate adsorption onto zirconium-modified bentonite. *J. Environ. Manage.* **2018**, *217*, 183−195.
(106) Venkiteshwaran, K.; Wells, E.; Mayer, B. K. Kinetics, Affinity, Thermodynamics, and Selectivity of Phosphate Removal Using Immobilized Phosphate-Binding Proteins. *Environ. Sci. Technol.* **2020**, *54*, 10885−10894.
(107) Bai, L.; Yuan, L.; Ji, Y.; Yan, H. Effective Removal of Phosphate from Aqueous by Graphene Oxide Decorated with α-Fe2O3: Kinetic, Isotherm, Thermodynamic and Mechanism Study. *Arabian J. Sci. Eng.* **2018**, *43*, 3611−3620.
(108) Yaghoobi-Rahni, S.; Rezaei, B.; Mirghaffari, N. Bentonite surface modification and characterization for high selective phosphate adsorption from aqueous media and its application for wastewater treatments. *J. Water Reuse Desalin.* **2017**, *7*, 175−186.
(109) Yao, S.; Wang, M.; Liu, J.; Tang, S.; Chen, H.; Guo, T.; Yang, G.; Chen, Y. Removal of phosphate from aqueous solution by sewage sludge-based activated carbon loaded with pyrolusite. *J. Water Reuse Desalin.* **2018**, *8*, 192−201.
(110) Wang, N.; Feng, J.; Chen, J.; Wang, J.; Yan, W. Adsorption mechanism of phosphate by polyaniline/TiO2 composite from wastewater. *Chem. Eng. J.* **2017**, *316*, 33−40.
(111) Xu, X.; Wang, B.; Tang, H.; Jin, Z.; Mao, Y.; Huang, T. Removal of phosphate from wastewater by modified bentonite entrapped in Ca-alginate beads. *J. Environ. Manage.* **2020**, *260*, 110130.
(112) Xiong, W.; Tong, J.; Yang, Z.; Zeng, G.; Zhou, Y.; Wang, D.; Song, P.; Xu, R.; Zhang, C.; Cheng, M. Adsorption of phosphate from aqueous solution using iron-zirconium modified activated carbon nanofiber: Performance and mechanism. *J. Colloid Interface Sci.* **2017**, *493*, 17−23.
(113) Li, J.; Li, B.; Huang, H.; Lv, X.; Zhao, N.; Guo, G.; Zhang, D. Removal of phosphate from aqueous solution by dolomite-modified biochar derived from urban dewatered sewage sludge. *Sci. Total Environ.* **2019**, *687*, 460−469.
(114) Sakulpaisan, S.; Vongsetskul, T.; Reamouppaturm, S.; Luangkachao, J.; Tantirungrotechai, J.; Tangboriboonrat, P. Titania-functionalized graphene oxide for an efficient adsorptive removal of phosphate ions. *J. Environ. Manage.* **2016**, *167*, 99−104.
(115) Vakili, M.; Deng, S.; Shen, L.; Shan, D.; Liu, D.; Yu, G. Regeneration of Chitosan-Based Adsorbents for Eliminating Dyes from Aqueous Solutions. *Sep. Purif. Rev.* **2019**, *48*, 1−13.
(116) Ma, H.; Xu, Z.; Wang, W.; Gao, X.; Ma, H. Adsorption and regeneration of leaf-based biochar for p-nitrophenol adsorption from aqueous solution. *RSC Adv.* **2019**, *9*, 39282−39293.
(117) Tahmasebi, E. Insights into the adsorption mechanism of Al30 polyoxocations-modified graphene oxide nanosheets for efficient removal of phosphate, chromate and selenate oxyanions: A comparative study. *J. Mol. Liq.* **2020**, *299*, 112111.
(118) Bakry, A. M.; Alamier, W. M.; Salama, R. S.; Samy El-Shall, M.; Awad, F. S. Remediation of water containing phosphate using

https://doi.org/10.1021/acsomega.2c05985
ACS Omega 2022, 7, 45386−45402

ceria nanoparticles decorated partially reduced graphene oxide (CeO2-PRGO) composite. *Surf. Interfaces* **2022**, *31*, 102006.
(119) Zheng, Q.; Yang, L.; Song, D.; Zhang, S.; Wu, H.; Li, S.; Wang, X. High adsorption capacity of Mg−Al-modified biochar for phosphate and its potential for phosphate interception in soil. *Chemosphere* **2020**, *259*, 127469.
(120) Zhang, Y.; Akindolie, M. S.; Tian, X.; Wu, B.; Hu, Q.; Jiang, Z.; Wang, L.; Tao, Y.; Cao, B.; Qu, J. Enhanced phosphate scavenging with effective recovery by magnetic porous biochar supported $La(OH)_3$: Kinetics, isotherms, mechanisms and applications for water and real wastewater. *Bioresour. Technol.* **2021**, *319*, 124232.
(121) Kugimiya, A.; Takei, H. Selective recovery of phosphate from river water using molecularly imprinted polymers. *Anal. Lett.* **2008**, *41*, 302−311.

https://doi.org/10.1021/acsomega.2c05985
ACS Omega 2022, 7, 45386−45402